Article

Regression of the Rician Noise Level in 3D Magnetic Resonance Images from the Distribution of the First Significant Digit

Rosa Maza-Quiroga [1,2,†] , Karl Thurnhofer-Hemsi [1,2,†] , Domingo López-Rodríguez [2,3,†] and Ezequiel López-Rubio [1,2,*,†]

1   Department of Computer Languages and Computer Science, Universidad de Málaga, Bulevar Louis Pasteur, 35, 29071 Málaga, Spain; rosammq@lcc.uma.es (R.M.-Q.); karlkhader@lcc.uma.es (K.T.-H.)
2   Instituto de Investigación Biomédica de Málaga y Plataforma en Nanomedicina-IBIMA Plataforma Bionand, 29590 Malaga, Spain
3   Department of Applied Mathematics, Universidad de Málaga, Bulevar Louis Pasteur, 35, 29071 Málaga, Spain; dominlopez@uma.es
*   Correspondence: ezeqlr@lcc.uma.es; Tel.: +34-952-137155
†   These authors contributed equally to this work.

Abstract: This paper investigates the distribution characteristics of Fourier, discrete cosine, and discrete sine transform coefficients in T1 MRI images. This paper reveals their adherence to Benford's law, characterized by a logarithmic distribution of first digits. The impact of Rician noise on the first digit distribution is examined, which causes deviations from the ideal distribution. A novel methodology is proposed for noise level estimation, employing metrics such as the Bhattacharyya distance, Kullback–Leibler divergence, total variation distance, Hellinger distance, and Jensen–Shannon divergence. Supervised learning techniques utilize these metrics as regressors. Evaluations on MRI scans from several datasets coming from a wide range of different acquisition devices of 1.5 T and 3 T, comprising hundreds of patients, validate the adherence of noiseless T1 MRI frequency domain coefficients to Benford's law. Through rigorous experimentation, our methodology has demonstrated competitiveness with established noise estimation techniques, even surpassing them in numerous conducted experiments. This research empirically supports the application of Benford's law in transforms, offering a reliable approach for noise estimation in denoising algorithms and advancing image quality assessment.

Keywords: MRI; Rician noise; Benford's law; noise level estimation

MSC: 68U10; 62H35

1. Introduction

Rician noise appears in various fields and applications: in wireless communications systems [1,2], Rician noise arises due to the presence of multipath fading; in radar systems [3], this type of noise can be present in signals due to the interaction of the transmitted radar signal with objects and the surrounding environment; in optical communication systems [4], the interference between the direct signal and reflected or scattered components can introduce Rician noise; and in magnetic resonance imaging (MRI) [5], the noise is present when the MRI signal from protons in tissues interferes constructively or destructively, leading to the presence of both signal and noise components in the acquired image.

As a widely used diagnostic tool, MRI provides detailed information about internal organs, tissues, and abnormalities that may not be easily discernible through other imaging modalities. The clinical implications of MRI cannot be understated, as it plays a vital role in various medical disciplines, such as neurology, oncology, and musculoskeletal imaging. Therefore, understanding the characteristics of Rician noise in MRI images is of utmost

importance, as noise can significantly impact the quality and accuracy of these diagnostic images, potentially leading to misinterpretations or missed diagnoses.

Moreover, Rician noise presents specific challenges in MRI images that are distinct from other types of noise encountered in different imaging modalities. Rician noise is known to be signal-dependent, making it challenging to separate noise from the raw MRI data while preserving important image features, and it affects low-intensity regions, which are crucial for detecting subtle abnormalities or lesions. Accurate estimation of the deviation parameter of the Rician noise distribution is essential for developing effective denoising techniques and improving image quality, directly benefiting clinical diagnosis, treatment planning, and monitoring.

Denoising methods are an essential aspect of pre-processing for magnetic resonance imaging (MRI), and their goal is to improve image quality by increasing the signal-to-noise ratio (SNR) while preserving the essential features of the image. A wide variety of denoising methods have been proposed in the literature, including those based on the wavelet transform [6], anisotropic diffusion filter [7], maximum likelihood approach [8], linear minimum square error [9], singular value decomposition [10], sparse representation learning [11], non-local filters [12], and variational mode decomposition [13].

With the advent of deep learning, new denoising techniques have emerged that have shown to be highly effective at addressing the noise component in MRI data. One such technique is the use of stacked sparse auto-encoders, as proposed in [14], which uses a stacked architecture of sparse auto-encoders to learn a compact and robust representation of the data. Another technique is the use of multi-layer perceptrons, as presented in [15], which utilizes a deep neural network architecture to learn a non-linear mapping between the noisy and clean images. Additionally, convolutional neural networks (CNNs) have been proposed for medical image denoising [16], which have been shown to effectively learn the underlying image structure and remove noise. Furthermore, attention-guided models such as [17] have been presented, which use attention mechanisms to selectively focus on the regions of the image that are most affected by noise. These deep learning-based methods have been shown to achieve good performance in denoising MRI data, particularly in the case of the residual learning-based deep denoising conventional neural network for Gaussian denoising [18] and the convolutional neural network for medical image denoising [19]. These methods have been shown to be effective at removing noise while preserving image features, resulting in higher-quality images and improved diagnostic accuracy. Moreover, a recent study demonstrated that denoising using a deep neural network performs better than several conventional denoising methods [20].

Some denoising algorithms assume knowledge of the deviation parameter σ of the Rician distribution that generates the noise. This parameter is crucial for the performance of the denoising algorithm as it characterizes the level of noise present in the image. Estimation of this noise parameter can be achieved through methods based on the principal components analysis (PCA) [21] and wavelet transform [22]. The PCA-based method is more effective for weak texture images as it is based on the analysis of the principal components of the data, but it is less suited for Rician noise estimation as it assumes a Gaussian distribution. In the wavelet approach, the image is decomposed into sub-bands, with the HH sub-band consisting of the wavelet noise coefficients. The median of these coefficients is then utilized to compute the *median absolute deviation* estimator for σ, which is a robust statistic for estimating the noise level. Although this wavelet model is more suitable for Gaussian noise, it can be appropriately modified [23] for estimating the σ parameter in Rician noise. This is accomplished by exploiting the characteristics of the Rician distribution, such as the presence of a non-zero mean, and using them to adapt the estimation process accordingly.

In this study, we propose an alternative method for estimating the noise deviation parameter by analyzing the statistical distribution of the first significant digits in a dataset using Benford's law. While it is commonly acknowledged that the histogram of an image does not conform to Benford's law, certain image transformations have been found to

exhibit consistency with this distribution. For example, in [24], it was demonstrated that the gradient and Laplace transform magnitude adhere to Benford's law, even in medical images such as MRI [25]. Additionally, other transformations, such as the discrete cosine and wavelet transforms [26], have been found to have coefficients that conform to Benford's law. The proposed method leverages these findings to analyze the coefficients of different transforms of an image and determine the level of agreement between the expected distribution and the actual first digit distribution in the transformed domain as an indicator of the noise parameter σ. Through this approach, the aim is to demonstrate that the transform coefficients of an image closely follow Benford's law and that larger amounts of noise in an image result in deviation from this distribution.

While it is true that Benford's law has been previously applied in various domains, including financial auditing [27], data analysis [28] and as quality-aware features in synthetic images [29], its application to estimate the noise deviation parameter in medical images, particularly in the context of MRI, is a novel contribution. This study demonstrates the use of Benford's law to analyze the statistical distribution of the first significant digits of image transform coefficients as an indicator of noise level. The novelty lies in the specific application of Benford's law to estimate the noise parameter σ in different image transforms. To the best of our knowledge, such an approach has not been previously explored for noise estimation in medical images.

It is shown how regression techniques can be applied to accurately predict the noise level of an image. Note that, in a previous work [30], the authors have explored the regression of the noise level from the fitting of the Fourier coefficients to Benford's law. Now, we provide a deeper study to assess if other different transforms (such as the *discrete cosine transform* and the *discrete sine transform*) present the same first-digit distribution.

This study demonstrates the effectiveness of the proposed method in estimating the noise deviation parameter across different image transforms. Comprehensive analyses, including comparisons with existing methods and an evaluation using diverse datasets, were carried out. The results showcase the consistent adherence of the first-digit distributions in transformed images to Benford's law, as well as the correlation between the deviations from this distribution and the noise level. These findings provide empirical evidence supporting the utility of the proposed method for accurate noise estimation.

This study is structured as follows. Following the introduction, Section 2 describes the proposed method in detail. In Section 3, the experimental setting and datasets used to test our hypothesis are described, and in Section 4, the experimental results are presented, including a comprehensive analysis of the results obtained. Finally, a conclusion is drawn in Section 5, summarizing the main findings of this research and highlighting potential areas for future work.

2. Methodology

Next, the proposal to estimate the level of Rician noise in 3D MRIs is detailed. As is known in the previous literature, the distribution of the noise for the magnitude of magnetic resonance images can be well modeled by the Rice probability distribution [5]. Let us note the noiseless voxel intensity as $\hat{x}$, while x is the measured (noisy) voxel intensity corrupted by Rician noise with level σ. Here, σ is the standard deviation of a Gaussian noise process that affects both the real part and imaginary part of the magnetic resonance image. Therefore, the noise level σ can be assumed to be equal for both parts. Under these conditions, the probability density of observing x is [5]:

$$p(x) = \frac{x}{\sigma^2} \exp\left(-\frac{x^2 + \hat{x}^2}{2\sigma^2}\right) \mathrm{I}_0\left(\frac{x\hat{x}}{\sigma^2}\right) \tag{1}$$

where I_0 stands for the modified zeroth-order Bessel function of the first kind.

We propose estimating the Rician noise level σ by comparing the observed distribution of the first significant digit with the probability distribution given by Benford's law. This is

an empirical law that establishes a logarithmic probability distribution $Q(m)$ for the first significant digit m of the base-10 representation of a non-null real number y [31]:

$$m = \left\lfloor \frac{|y|}{10^{\lfloor \log_{10}|y| \rfloor}} \right\rfloor \tag{2}$$

$$Q(m) = \log_{10}\left(1 + \frac{1}{m}\right) \tag{3}$$

where $m \in \{1, 2, \ldots, 9\}$, $|\cdot|$ denotes the absolute value, and $\lfloor \cdot \rfloor$ stands for rounding towards $-\infty$.

If a distribution of real numbers follows Benford's law, then most of them start with lower digits. In particular, the probability of starting with the digit 1 is about 0.301, digit 2 is about 0.176, and so on. The least likely starting digit is 9 with a probability of about 0.046. It is remarkable that many natural processes lead to number distributions that follow this law. These distributions include sizes of geographic features, numbers of individuals in a biological population, and specific heats of chemical compounds. In particular, those distributions that come from the combination of several factors or subprocesses are more likely to follow the law. It has been shown [32] that if random samples are drawn from a random collection of probability distributions that conform to some unbiasedness conditions, then the combined distribution of samples will conform to Benford's law.

Many empirical distributions coming from natural processes follow Benford's law [26]. We hypothesize that this is also the case for noiseless MRIs. In other words, the more Rician noise that an MRI contains, the more that it departs from Benford's law. Unfortunately, the distribution of the first significant digit is extremely sensitive to the scale of possible values, which is highly variable for MRIs. We propose alleviating this issue by considering the values of a 3D transform of the MRI intensity values. The scale of the transformed values is quite independent of the scale of intensity values, which makes the former more adequate for the analysis of the first significant digits than the latter. Moreover, it has been observed that probability distributions with a wide range, i.e., those that spread across many orders of magnitude, are more likely to obey Benford's law [33]. This is the case for some transforms. For example, the first digit distribution of the 2D discrete cosine transform coefficients according to Benford's law has been employed to detect fake images and repeated JPEG compressions [34–37]. The following multidimensional 3D transforms have been considered for this purpose: discrete Fourier transform (DFT), discrete cosine transform (DCT) type 2, and discrete sine transform (DST) type 2. They are defined as follows [38]:

$$y_{DFT,\mathbf{k}} = \sum_{\mathbf{n}=0}^{\mathbf{N}-\mathbf{u}} x_{\mathbf{k}} \exp(-i2\pi \mathbf{k} \cdot (\mathbf{n} \div \mathbf{N})) \tag{4}$$

$$y_{DCT,\mathbf{k}} = \sum_{\mathbf{n}=0}^{\mathbf{N}-\mathbf{u}} x_{\mathbf{k}} \cos\left(\frac{\pi}{2}\mathbf{k} \cdot ((2\mathbf{n} + \mathbf{u}) \div \mathbf{N})\right) \tag{5}$$

$$y_{DST,\mathbf{k}} = 2 \sum_{\mathbf{n}=0}^{\mathbf{N}-\mathbf{u}} x_{\mathbf{k}} \sin\left(\pi(\mathbf{k} + \mathbf{u}) \cdot \left(\left(\mathbf{n} + \frac{1}{2}\mathbf{u}\right) \div \mathbf{N}\right)\right) \tag{6}$$

where $\cdot$ stands for the dot product, i denotes the imaginary unit, $\mathbf{u} = (1, 1, 1)$, and $\mathbf{k} = (k_1, k_2, k_3)$ and $\mathbf{n} = (n_1, n_2, n_3)$ are three-dimensional index vectors. The j-th component of $\mathbf{k}$ and $\mathbf{n}$ has values ranging from 0 to $N_j - 1$, where N_j is the number of voxels of the images in the j-th dimension, $j \in \{1, 2, 3\}$. Also, $\mathbf{N} = (N_1, N_2, N_3)$. Finally, $\mathbf{n} \div \mathbf{N}$ stands for the element-wise division of three-dimensional vectors:

$$\mathbf{n} \div \mathbf{N} = \left(\frac{n_1}{N_1}, \frac{n_2}{N_2}, \frac{n_3}{N_3}\right) \tag{7}$$

From now on, we will note y as the result of applying one of the 3D considered transforms (DFT, DCT, or DST) to the measured pixel intensity values x. The first significant digit of the representation of y in decimal format will be noted as m, as defined in (2).

Let $P(m)$ be the observed probability distribution of m, and let $Q(m)$ be the theoretical probability distribution of m as obtained from Benford's law (3). The dissimilarity between the probability distributions $P(m)$ and $Q(m)$ must be measured in order to be employed as an input for the regression of the Rician noise level σ. The lower the dissimilarity, the lower the Rician noise level. The following measures are considered: Bhattacharyya distance (BD), Kullback–Leibler divergence (KL), total variation distance (TV), Hellinger distance (HD), and Jensen–Shannon divergence (JS). They are defined as follows [39–43]:

$$\mathcal{D}_{BD}(P,Q) = -\log \sum_{m=1}^{9} \sqrt{P(m)Q(m)} \tag{8}$$

$$\mathcal{D}_{KL}(P,Q) = \sum_{m=1}^{9} P(m) \log \frac{P(m)}{Q(m)} \tag{9}$$

$$\mathcal{D}_{TV}(P,Q) = \max_{m \in \{1,\dots,9\}} |P(m) - Q(m)| \tag{10}$$

$$\mathcal{D}_{HD}(P,Q) = \frac{1}{\sqrt{2}} \sqrt{\sum_{m=1}^{9} \left(\sqrt{P(m)} - \sqrt{Q(m)} \right)^2} \tag{11}$$

$$\mathcal{D}_{JS}(P,Q) = \frac{1}{2} \mathcal{D}_{KL}(P,V) + \frac{1}{2} \mathcal{D}_{KL}(Q,V) \tag{12}$$

where

$$V = \frac{1}{2}(P + Q) \tag{13}$$

The Rician noise level σ is estimated from them by means of a regression function f applied to H dissimilarity measures:

$$\sigma \approx f(\varphi_1(P,Q), \dots, \varphi_H(P,Q)) \tag{14}$$

$$\varphi_h \in \{\mathcal{D}_{BD}, \mathcal{D}_{KL}, \mathcal{D}_{TV}, \mathcal{D}_{HD}, \mathcal{D}_{JS}\} \ \forall h \in \{1, \dots, H\} \tag{15}$$

where f is obtained by machine learning regression methods from the observed dissimilarities (input variables or *predictors*) and the actual Rician noise level (output variable). In this work, one input variable ($H = 1$) and two input variables ($H = 2$) have been considered for the regression. The following regression methods have been considered: linear regression, polynomial (quadratic) regression, random forest regression, support vector regression, and kernel regression.

After the regression function f has been learned from the data, the performance of the estimation (14) must be measured. To this end, three performance measures have been chosen: the mean square error (MSE; lower is better), the mean absolute error (MAE; lower is better), and the coefficient of determination (R^2; higher is better). Their definitions are as follows:

$$MSE = \frac{1}{T} \sum_{t=1}^{T} (\sigma_t - f(\varphi_1(P_t, Q), \dots, \varphi_H(P_t, Q)))^2 \tag{16}$$

$$MAE = \frac{1}{T} \sum_{t=1}^{T} |\sigma_t - f(\varphi_1(P_t, Q), \dots, \varphi_H(P_t, Q))| \tag{17}$$

$$R^2 = 1 - \frac{MSE}{\frac{1}{T} \sum_{t=1}^{T} (\sigma_t - \hat{\sigma})^2} \tag{18}$$

$$\hat{\sigma} = \frac{1}{T} \sum_{t=1}^{T} \sigma_t \tag{19}$$

where σ_t is the actual noise level of the test image of index t and T is the total number of test images.

Outlined in this section are the steps executed by the algorithm presented in Figure 1. Hereafter, the algorithm's procedure is elucidated:

1. A 3D MRI image belonging to a repository is selected.
2. Each image renders 20 noisy images.
3. Three transformations are applied to each noisy image: DFT, DCT, and DST, providing three transformed noisy images.
4. Calculate the distribution of the appearance of the first significant digit for each transformed noisy image.
5. The distribution obtained is compared with Benford's law distribution using five divergences: BD, KL, TV, H, and JS.
6. Each combination of transform and divergence measure gives place to a metrics set that will be used to predict the noise added to the image.
7. Different regressors are used to train and validate models with either one or two inputs (metrics).
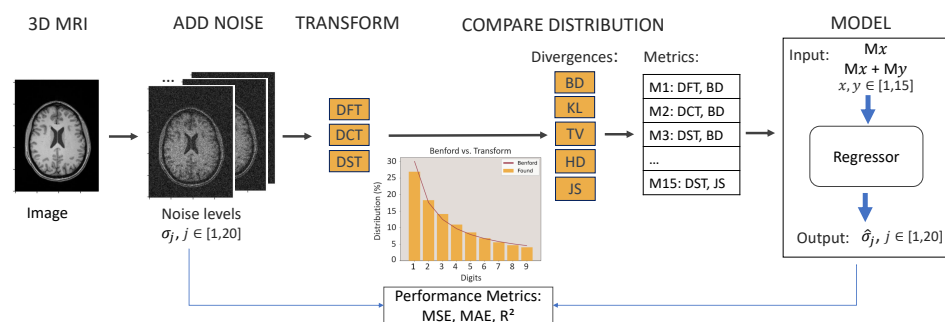8. To evaluate the precision of each model, three performance metrics are used: MSE, MAE, and R^2.

Figure 1. From left to right, the steps of the algorithm are presented. Images from each repository are noise-added. The noise image is transformed, and the distribution of the first digit appearance is compared with Benford's Law distribution. The couple transform divergence makes one metric (M_x) that will be used as an input on the model. The input can be single or double, and the output is the predicted noise on the image. Three performance metrics are used to measure the success of the model.

3. Experimental Settings

To assess the validity of our methodology, the experiments were conducted on very different datasets. We made sure that the selected repositories were publicly available to allow replication. Furthermore, we selected datasets with high dimensionality and discarded those with insufficient dimensional resolution in any of the axes, which is common in some image modalities. In this way, we ensure a sufficient number of voxels to generate the Benford distribution. First, 95 T1-weighted brain MRIs were carefully selected from healthy participants through Mindboggle [44] to ensure high quality for an accurate noise analysis. These images are publicly accessible with a non-restrictive license. Also, 903 images from fastMRI [45] were used. The data, including the number of MRIs and their dimensions (in parentheses), are described below. For sub-datasets in which dimension is not specified, the number of slices of the first and second dimensions vary in the interval $[192, 512]$ and $[256, 512]$, respectively, while the third dimension takes the value 16.

For Mindboggle, the NIfTI format images were obtained from five repositories: HLN [46] $(12, 256 \times 256 \times 170)$, MMRR [47] $(21, 170 \times 256 \times 256)$, NKI-RS [48] $(22, 192 \times 256 \times 256)$, NKI-TRT [48] $(20, 192 \times 256 \times 256)$, and OASIS-TRT [49] $(20, 256 \times 256 \times 160)$.

For fastMRI, the NIfTI format images were obtained from eight data subsets: five data subsets with 1.5 Tesla acquisitions, hereinafter fastMIR-1.5; and three data subsets with 3 Tesla acquisitions, hereinafter fastMIR-3. fastMIR-1.5 is composed of the sub-datasets AX-T1-1.5 (210), AX-T1-POST-1.5 (219), Axial-T1-SE (12), T1-AXIAL (13), and T1-AXIAL-POST-GAD (22). fastMIR-3 is composed of the sub-datasets AX-T1-3 (134), AX-T1-FLASH-POST (22), and AX-T1-POST-3 (267).

In order to simulate Rician Noise, a normal distribution was generated utilizing the standard deviation within the specific range $(0\%, 40\%]$ to control the variability of the noise. Then, the Gaussian noise was added in the complex domain by scaling with respect to the amplitude of the signal [50]:

$$I_r = \hat{X} + s\mu_1, \ \mu_1 \sim \mathcal{N}(0, \sigma_j), \qquad I_i = \hat{X} + s\mu_2, \ \mu_2 \sim \mathcal{N}(0, \sigma_j), \qquad s = IQR(\hat{X}) \quad (20)$$

$$X_j = \sqrt{I_r^2 + I_i^2} \quad (21)$$

where $\hat{X}$ is the original image, I_r and I_i are the real and imaginary component, σ_j is the standard deviation of the added Gaussian noise, s is a noise scaling parameter, and X is the computed noisy image. For each T1 image, $j = 20$ random noisy images were generated with $\sigma_j \in (0, 0.4]$, each with its unique noise pattern for each repository. This process allowed us to create diverse images with controlled noise levels. The interquartile range is employed as the noise-scaling parameter. This way, the added noise level is robust against outliers in the values of the noiseless images. To complete this explanation, in Table 1, we list the SNR values obtained after adding noise at different levels of σ.

Table 1. Noise levels (σ) used in this work and the induced SNR of the noisy images in the 12HLN repository.

σ	Average SNR	σ	Average SNR
0.02	521.80	0.22	5.30
0.04	131.19	0.24	4.62
0.06	58.86	0.26	4.08
0.08	33.55	0.28	3.66
0.10	21.83	0.30	3.31
0.12	15.47	0.32	3.03
0.14	11.63	0.34	2.80
0.16	9.14	0.36	2.61
0.18	7.43	0.38	2.44
0.20	6.21	0.40	2.30

Subsequently, the transformations were computed using all MRI voxels, and a probability distribution of the frequency of the first digit for each voxel was constructed. Afterwards, all the images in the transformed domain were evaluated to ensure that they fit Benford's law distribution.

Considering Benford's law as a noise detection mechanism, five different models were put forward to predict the quantity of noise in an MRI:

- Linear regression (LR): fits a straight line to data points to model linear relationships.
- Polynomial regression of degree two (PR): extends linear regression by using quadratic functions to capture non-linear patterns.
- Random forest (RF): ensemble of decision trees that provides a flexible, non-linear regression model.
- Support vector regression (SVR): uses support vector machines to find a hyperplane that best fits the data while allowing for deviations.
- Kernel regression (KR): applies kernel functions to estimate non-linear relationships between data points.

Some of the following parameters were set to train the models, and the rest were kept at their default values:

- PR: the maximal degree of the polynomial features is two, and no bias (i.e., like intercept in LR) was included (*include_bias = False*).
- RF: the minimum number of samples required to split an internal node is 20 (*min_samples_split = 20*).
- SVR: *rbf* kernel was employed with regularization parameter $C = 1$ and *epsilon* = 0.001.
- KR: the type of variable was set as continuous, multiplied by the total number of features.

A 10-fold cross-validation was used to evaluate the models for each repository separately. Therefore, the images from each repository were split into training (90%) and validation (10%) sets 10 times to validate the considered models. *MSE*, *MAE*, and R^2 were the performance metrics used to measure the agreement between the predicted noise and the actually added noise, following Equations (16)–(18). *MSE* and *MAE* measure the squared and absolute errors, respectively, and R^2 indicates the goodness-of-fit of the predicted noise in the test images.

For the present investigation, up to two metrics were utilized as inputs for each regressor, and the output is always the noise quantity/level. The considered metrics are listed in Table 2. The notation **Mi** is employed whenever the *i*-th metric is employed as the only input for the regression. On the other hand, the notation **Mi + Mj** means that the *i*-th and *j*-th metrics are used as joint inputs for the regression; that is, the predictor variables in the regression model are given by the vector (**Mi, Mj**). Joint metrics are employed because in many cases, two inputs provide more information than one to the regressor, thereby leading to better Rician noise estimation performance. There are 120 metrics analyzed: 15 **Mi** and 105 **Mi + Mj**. The considered metrics span a wide range of fast 3D transformations, and the probability distribution dissimilarity measures are conducted so as to increase the options to obtain a good estimation of the Rician noise from the study of the dissimilarity of the first digit distribution of the transformed data with respect to the Benford distribution. Please note that in the experiments, good results are attained with different dissimilarity measures. Therefore, dropping some of them would somehow decrease the performance of the proposed noise estimation approach. These dissimilarity measures have been chosen because they are fast to compute and are well known in the probability distribution dissimilarity literature.

Table 2. Definitions of metric variables, specifying the transformation and dissimilarity measures used.

Metrics	Transformation	Dissimilarity
M1	DFT	BD
M2	DCT	BD
M3	DST	BD
M4	DFT	KL
M5	DCT	KL
M6	DST	KL
M7	DFT	TV
M8	DCT	TV
M9	DST	TV
M10	DFT	HD
M11	DCT	HD
M12	DST	HD
M13	DFT	JS
M14	DCT	JS
M15	DST	JS

When employing a single metric as the input, the results are depicted in Figures 2 and S1–S13. These figures illustrate the models (represented by color lines) and their alignment with the data points (depicted as blue dots) for diverse sub-datasets, highlighting the best metric for each specific case.
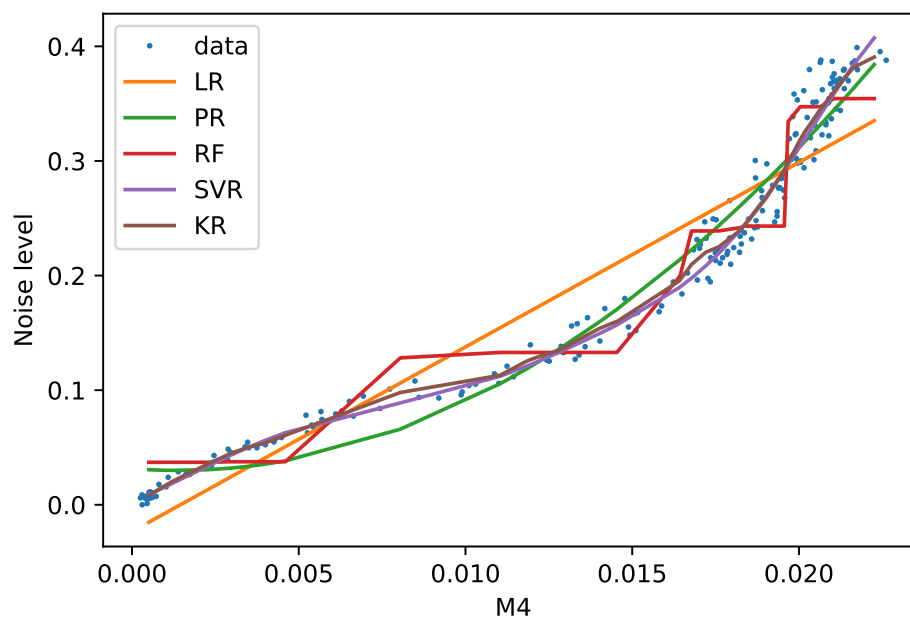
Figure 2. M4 training data (blue dots) are displayed along with the five models in the HLN repository.

After extensive research, the variance-stabilizing transformation (VST) [51] methodology is the only one with publicly available code; therefore, this method has been used to compare with our models. They present a stable and fast iterative procedure for robustly estimating the noise level from a single Rician-distributed image. The results of predicting the Rician noise with the proposed procedure were compared based on the performance measures for each sub-dataset.

For this study, we used a PC with an Intel Core i7 CPU, 32 GB of RAM, an NVIDIA RTX2080 Super Ventus GPU, and a 1TB SSD. The system operated on Ubuntu 20.04 and utilized Python 3.8, along with various scientific libraries, including *matplotlib*, *nibabel*, *scipy*, *sklearn*, and *benford* [52]. The source code with the scripts and sample data is available at: https://github.com/icai-uma/Regression_RicianNoiseLevel_3DMRI_DistributionFirstSignificantDigit (accessed on 3 September 2023).

4. Results

In a previous work [30], we explored only M1 and M3 as separate inputs for the regression of the Rician noise level, obtaining the best results in the PR model with the HLN repository. Now, we propose new metrics as inputs and new regressors to estimate the Rician noise.

There are 120 different metrics analyzed in this study (15 single metrics and 105 combinations of two metrics). The metrics are evaluated by three performance measures (MSE, MAE, and R^2). For each repository and sub-dataset and for each performance measure, a score is assigned to every metric. The best performing metric is given a score of 120, the second best a score of 119, and so on. For the Mindboggle and fastMRI (1.5 T acquisition) repositories, five sub-datasets are considered; hence, the maximum score of a metric in those repositories is 600, so the closer it is to this value, the better the metric performs on the repository. In the fastMRI 3T acquisition repository, only three sub-datasets were considered; thus, the maximum possible score for a metric in this repository is 360.

Note that in the tables, we present the three goodness-of-fit measures used in this work for each of the repositories used, presenting only the 10 best sets of predictors after scoring by aggregating the experimental results for each repository.

This analysis was carried out for each sub-dataset, presented in the Supplementary Materials: for HLN, see Tables S1–S3; for MMRR, see Tables S4–S6; for NKI-RS, see Tables S7–S9; for NKI-TRT, see Tables S10–S12; for OASIS-TRT, see Tables S13–S15;

for AX-T1-1.5, see Tables S16–S18; for AX-T1-POST-1.5, see Tables S19–S21; for Axial-T1-SE, see Tables S22–S24; for T1-AXIAL, see Tables S25–S27; for T1-AXIAL-POST-GAD, see Tables S28–S30; for AX-T1-3, see Tables S31–S33; for AX-T1-FLASH-POST, see Tables S34–S36; and for AX-T1-POST-3, see Tables S37–S39. To make this information collected in the tables in the Supplementary Materials understandable, this paper includes one figure for each dataset plotting the best input: for one metric as an input, see Figure 2; and for two metrics as an input, see Figures 3–14. The metrics were selected according to the R^2 value based on the analysis represented in the Supplementary Materials.

Figure 2 shows the graphical representation of the linear regression models obtained using the M4 metric as the only predictor. The blue points indicate the values of the training set, while the colored lines represent each of the estimates made by the different models.
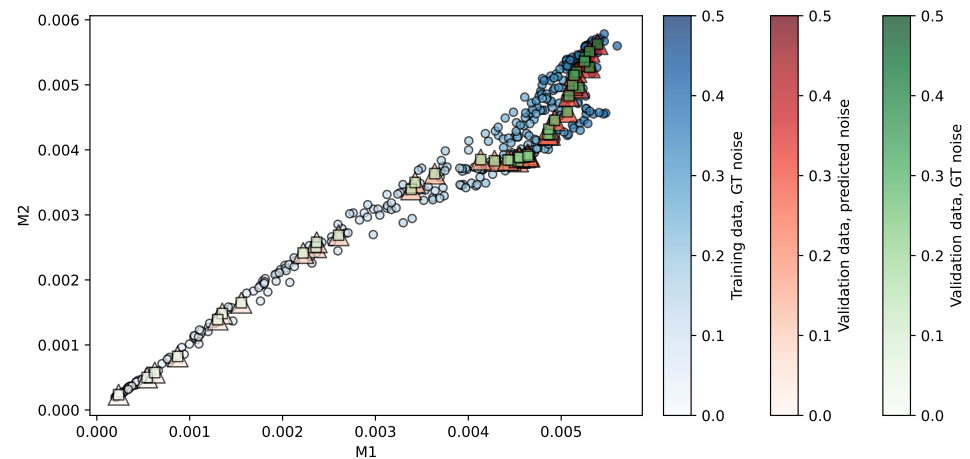

Figure 3. Regression of the MMRR repository using SVR. Predictors are (M1, M2). The opacity of each shape indicates the noise level associated. More details in the main text.
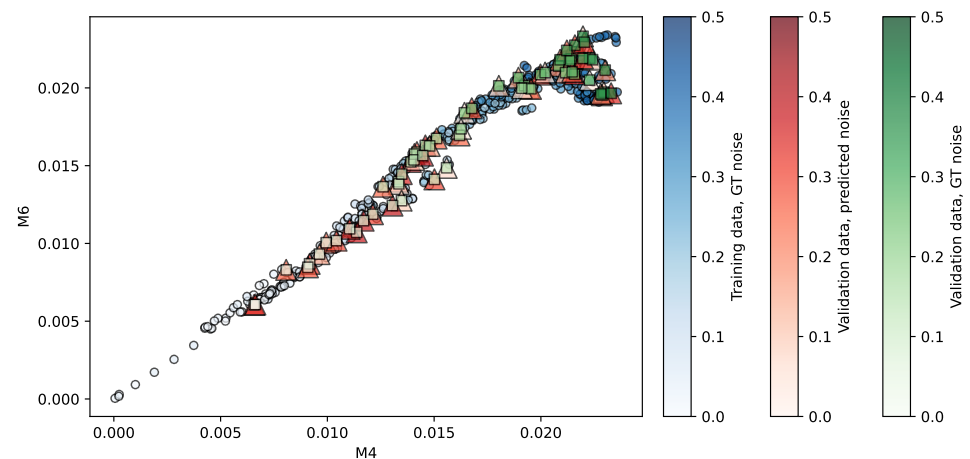

Figure 4. Regression of the NKI-RS repository using PR. Predictors are (M4, M6). The opacity of each shape indicates the noise level associated.
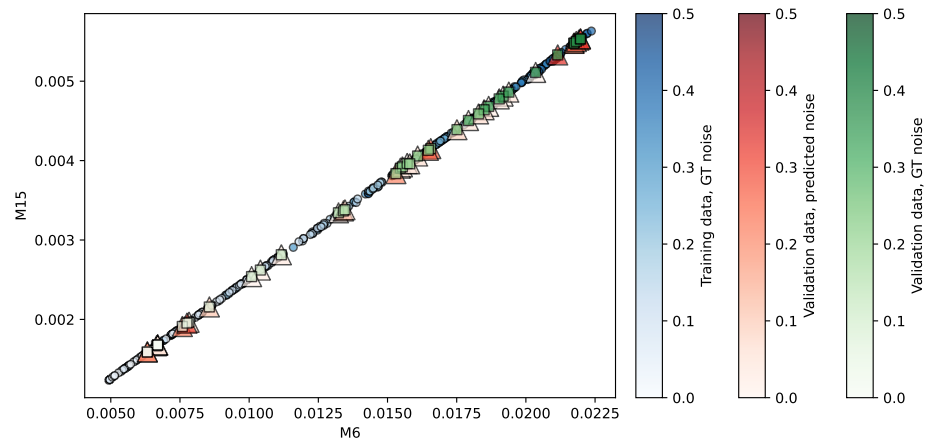
Figure 5. Regression of the NKI-TRT repository using LR. Predictors are (M6, M15). The opacity of each shape indicates the noise level associated.
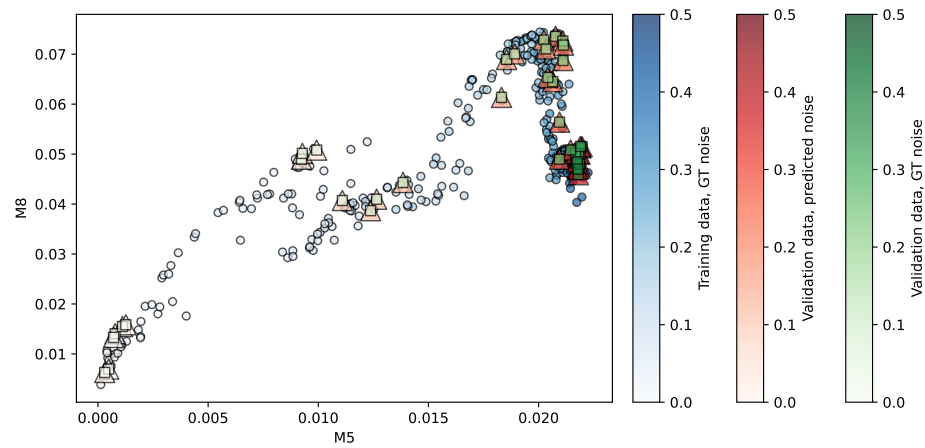

Figure 6. Regression of the OASIS-TRT repository using KR. Predictors are (M5, M8). The opacity of each shape indicates the noise level associated.
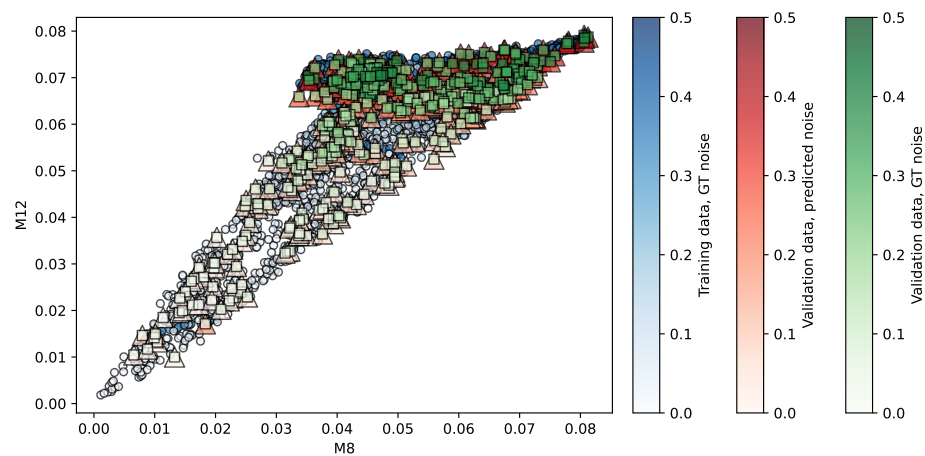

Figure 7. Regression of the AX-T1 dataset with 1.5 Tesla acquisition using KR. Predictors are (M8, M12). The opacity of each shape indicates the noise level associated.
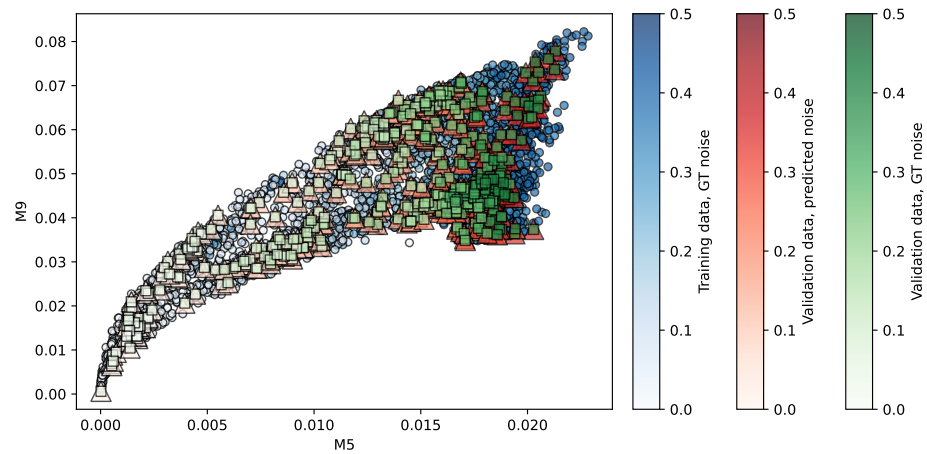
Figure 8. Regression of the AX-T1-POST dataset with 1.5 Tesla acquisition using SVR. Predictors are $(M5, M9)$. The opacity of each shape indicates the noise level associated.
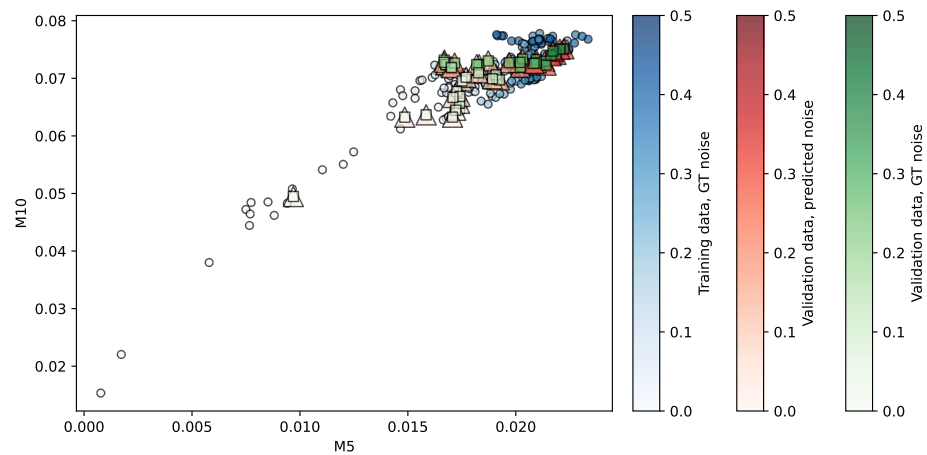

Figure 9. Regression of the AX-T1-SE dataset with 1.5 Tesla acquisition using SVR. Predictors are $(M5, M10)$. The opacity of each shape indicates the noise level associated.
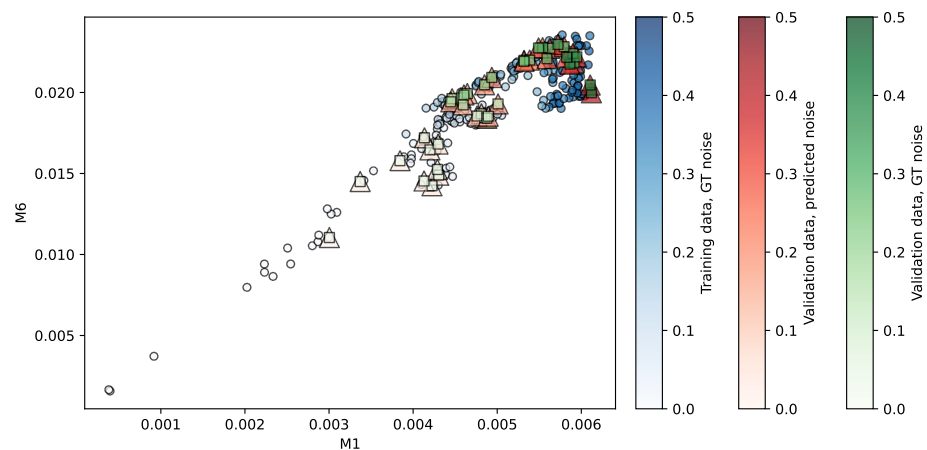

Figure 10. Regression of the T1-AXIAL dataset with 1.5 Tesla acquisition using KR. Predictors are $(M1, M6)$. The opacity of each shape indicates the noise level associated.
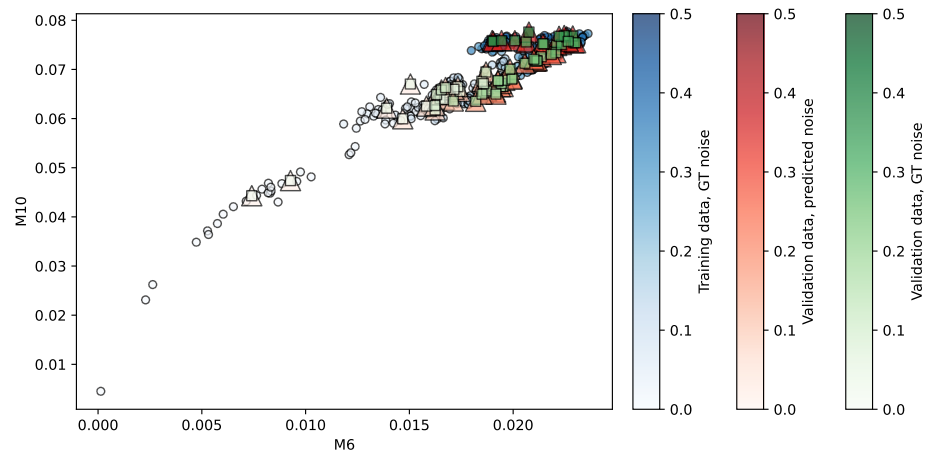
Figure 11. Regression of the AXIAL-POST-GAD dataset with 1.5 Tesla acquisition using KR. Predictors are (M6, M10). The opacity of each shape indicates the noise level associated.
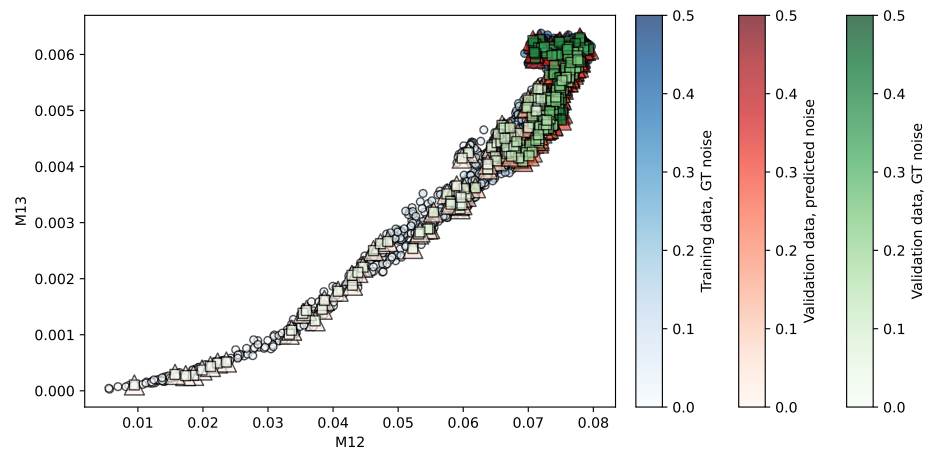

Figure 12. Regression of the AX-T1 dataset using KR (best ranked model). Predictors are (M12, M13). The opacity of each shape indicates the noise level associated.
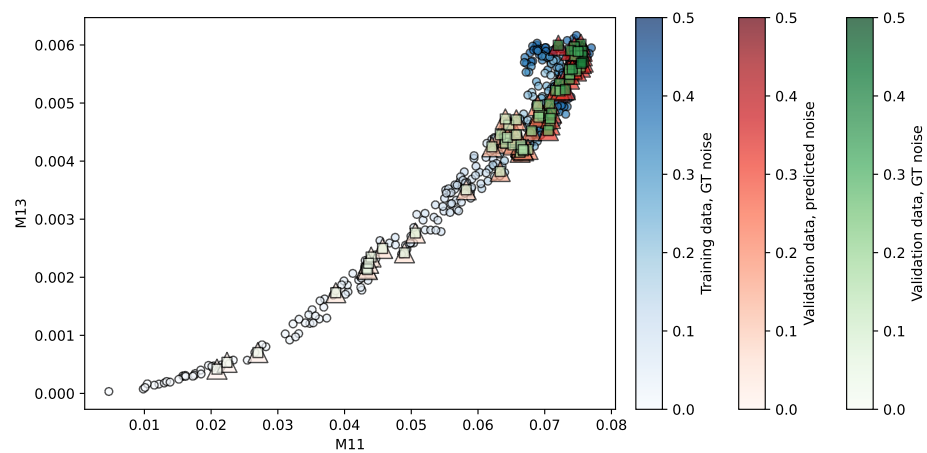

Figure 13. Regression of the AX-T1-FLASH-POST dataset using KR (best ranked model). Predictors are (M11, M13). The opacity of each shape indicates the noise level associated.
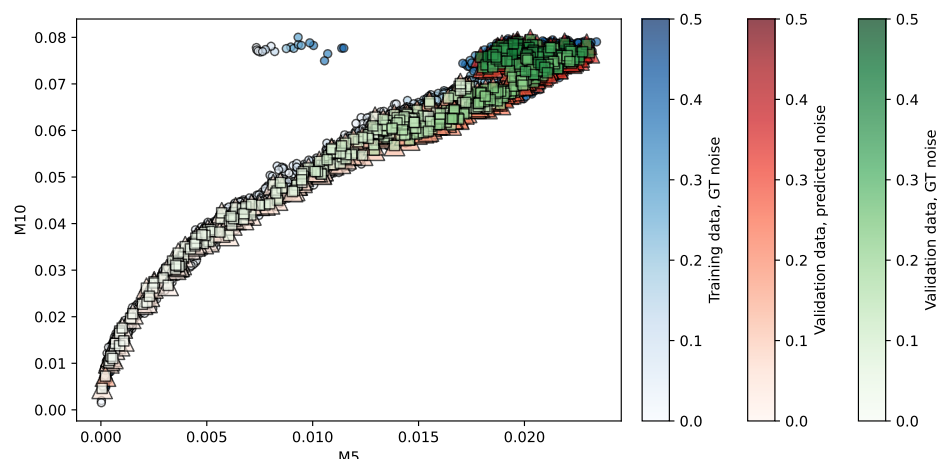
Figure 14. Regression of the AX-T1-POST dataset using KR (best ranked model). Predictors are $(M5, M10)$. The opacity of each shape indicates the noise level associated.

In each of Figures 3–14, each shape represents an instance of the corresponding repository, while the filled color indicates the level of noise.

- The amount of noise in one of the instances of the training set is indicated by the intensity of the blue fill color of the circles.
- The intensity of the green color within the squares indicates the *actual* level of noise in an instance of the validation set.
- The red color fill within a triangle has been used to indicate the level of noise *predicted* or *estimated* by the regression.

These shapes are located in the plane at coordinate points that coincide with the metrics used as inputs to the regression. That is, for each image in the training set, the corresponding metrics are calculated. For the sake of simplicity, let us assume that these metrics are M1 and M2, and let us illustrate this using Figure 3 as an example. In the graph, a circle is represented at the coordinates $(M1, M2)$, and the intensity of the blue fill is proportional to the actual level of noise present in the image. Once the regression model is created, it is applied to the images in the validation set; for each image, its metrics are calculated, and a square is placed in the corresponding coordinates. The green fill in the square represents the actual level of noise in the image. The estimate of the noise level produced by the regression model is represented by a triangle, in the same coordinates (as it corresponds to the same image) as the square of the same instance and with a fill intensity proportional to the estimate obtained. Thus, to compare the goodness-of-fit of the regression, the intensity of the filling of the squares and triangles must be compared. For a good fit, this intensity will be similar. This way of presenting the results graphically allows us to locate all instances, in both training and validation, to check if the validation is a representative sample of all the data and to confirm the fit made.

This information is summarized in Tables 3–11, one for each performance measure by dataset; the first shows MSE, the second MAE, and the third R^2. The metrics are sorted by score from best to worst, and the top 10 are shown. For each dataset, the best regressor is indicated in brackets, giving rise to the performance measure collected in the table. Notice these tables show the score of the metrics and the corresponding performance measure. Therefore, the best metric may not correspond to the best performance measure.

The results are presented below regarding each dataset in each subsection. First, the Mindboggle dataset is presented, followed by fastMRI, which is divided into two datasets: fastMRI-1.5 and fastMRI-3. Finally, a summary of the Section 4 is presented.

Table 3. Goodness-of-fit of noise level regression in the Mindboggle dataset. The metrics are globally ranked by the *MSE* value. For the sake of readability, *MSE* is scaled up by a factor of 10^4 in this table. Best-performing regressors are in brackets.

Metrics	Score	HLN	MMRR	NKI-RS	NKI-TRT	OASIS-TRT
M1 + M3	473	3.04 (KR)	2.51 (SVR)	11.36 (PR)	37.16 (PR)	7.18 (RF)
M3 + M13	468	3.04 (KR)	2.50 (SVR)	11.35 (PR)	37.17 (PR)	7.28 (RF)
M1 + M15	468	3.04 (KR)	2.50 (SVR)	11.36 (PR)	37.17 (PR)	7.23 (RF)
M13 + M15	462	3.04 (KR)	2.51 (SVR)	11.35 (PR)	37.17 (PR)	7.23 (RF)
M3 + M4	456	3.21 (KR)	2.55 (SVR)	11.25 (PR)	37.21 (PR)	7.21 (KR)
M4 + M15	453	3.23 (KR)	2.54 (SVR)	11.13 (PR)	37.21 (PR)	7.22 (RF)
M2 + M4	445	3.25 (KR)	2.56 (SVR)	11.33 (PR)	37.58 (PR)	6.79 (KR)
M4 + M14	444	3.26 (KR)	2.55 (SVR)	11.34 (PR)	37.58 (PR)	6.84 (KR)
M1 + M2	433	3.02 (KR)	2.49 (SVR)	11.46 (PR)	37.53 (PR)	7.69 (SVR)
M13 + M14	432	3.02 (KR)	2.49 (SVR)	11.45 (PR)	37.54 (PR)	7.67 (SVR)

Table 4. Goodness-of-fit of noise level regression in the Mindboggle dataset. The metrics are globally ranked by the *MAE* value, scaled up by a factor of 10^3 in this table.

Metrics	Score	HLN	MMRR	NKI-RS	NKI-TRT	OASIS-TRT
M12 + M13	499	12.57 (PR)	10.95 (SVR)	26.36 (RF)	36.77 (SVR)	19.50 (KR)
M1 + M12	496	12.58 (PR)	10.92 (SVR)	26.39 (RF)	36.78 (SVR)	19.51 (KR)
M3 + M4	492	12.93 (SVR)	11.06 (SVR)	26.23 (RF)	36.82 (SVR)	18.97 (KR)
M4 + M15	488	12.92 (SVR)	11.04 (SVR)	26.33 (RF)	36.89 (SVR)	19.03 (KR)
M1 +M11	480	12.57 (PR)	10.97 (SVR)	26.71 (RF)	37.35 (SVR)	18.81 (KR)
M11 + M13	474	12.58 (PR)	10.99 (SVR)	26.75 (RF)	37.34 (SVR)	18.81 (KR)
M1 + M3	473	13.27 (SVR)	10.96 (SVR)	26.32 (RF)	36.68 (SVR)	19.80 (RF)
M3 + M13	470	13.21 (SVR)	10.95 (SVR)	26.19 (RF)	36.71 (SVR)	19.88 (RF)
M6 + M13	469	13.15 (KR)	11.05 (SVR)	26.50 (RF)	36.60 (SVR)	19.50 (KR)
M1 + M15	468	13.21 (KR)	10.95 (SVR)	26.34 (RF)	36.68 (SVR)	19.85 (RF)

Table 5. R^2 of the regression models on the Mindboggle dataset.

Metrics	Score	HLN	MMRR	NKI-RS	NKI-TRT	OASIS-TRT
M1 + M3	477	0.9785 (KR)	0.9821 (SVR)	0.9125 (PR)	0.6952 (PR)	0.9444 (RF)
M1 + M15	472	0.9785 (KR)	0.9822 (SVR)	0.9125 (PR)	0.6952 (PR)	0.9441 (RF)
M3 + M13	469	0.9785 (KR)	0.9822 (SVR)	0.9125 (PR)	0.6951 (PR)	0.9437 (RF)
M13 + M15	462	0.9785 (KR)	0.9821 (SVR)	0.9125 (PR)	0.6951 (PR)	0.9440 (RF)
M4 + M15	458	0.9774 (SVR)	0.9819 (SVR)	0.9133 (PR)	0.6944 (PR)	0.9443 (RF)
M3 + M4	456	0.9775 (KR)	0.9818 (SVR)	0.9133 (PR)	0.6944 (PR)	0.9443 (RF)
M4 + M14	442	0.9772 (KR)	0.9818 (SVR)	0.9127 (PR)	0.6914 (PR)	0.9463 (KR)
M2 + M4	442	0.9772 (KR)	0.9817 (SVR)	0.9127 (PR)	0.6914 (PR)	0.9466 (KR)
M1 + M11	436	0.9803 (PR)	0.9821 (SVR)	0.9085 (RF)	0.6880 (PR)	0.9462 (KR)
M11 + M13	436	0.9803 (PR)	0.9821 (SVR)	0.9084 (RF)	0.6880 (PR)	0.9462 (KR)

Table 6. Goodness-of-fit of noise level regression in the fastMRI dataset with 1.5 Tesla acquisition. The metrics are globally ranked by the *MSE* value, scaled up by a factor of 10^4 in this table.

Metrics	Score	T1_AXIAL_POST_GAD	Axial_T1_SE	T1_AXIAL	AX_T1_POST_15	AX_T1_15
M5 + M10	530	7.83 (KR)	20.71 (SVR)	9.56 (SVR)	17.92 (SVR)	35.95 (KR)
M2 + M10	527	8.06 (KR)	20.94 (SVR)	9.54 (SVR)	17.92 (SVR)	35.88 (KR)
M10 + M14	525	8.05 (KR)	20.96 (SVR)	9.53 (SVR)	17.92 (SVR)	35.89 (KR)
M1 + M5	518	8.21 (SVR)	21.57 (SVR)	9.45 (KR)	17.91 (SVR)	36.33 (RF)
M5 + M13	511	8.20 (SVR)	21.53 (SVR)	9.46 (KR)	17.92 (SVR)	36.36 (RF)

Table 6. *Cont.*

Metrics	Score	T1_AXIAL_POST_GAD	Axial_T1_SE	T1_AXIAL	AX_T1_POST_15	AX_T1_15
M1 + M6	488	7.86 (SVR)	23.10 (SVR)	9.13 (KR)	18.46 (SVR)	35.76 (RF)
M4 + M5	486	8.43 (SVR)	21.99 (SVR)	9.63 (SVR)	17.90 (SVR)	36.57 (RF)
M2 + M13	484	8.51 (SVR)	23.04 (SVR)	9.59 (SVR)	17.93 (SVR)	36.22 (RF)
M13 + M14	479	8.53 (SVR)	22.90 (SVR)	9.64 (SVR)	17.93 (SVR)	36.15 (RF)
M6 + M13	478	7.88 (SVR)	23.14 (SVR)	9.14 (KR)	18.45 (SVR)	35.90 (RF)

Table 7. Goodness-of-fit of noise level regression in the fastMRI dataset with 1.5 Tesla acquisition. The metrics are globally ranked by the *MAE* value, scaled up by a factor of 10^3 in this table.

Metrics	Score	T1_AXIAL_POST_GAD	Axial_T1_SE	T1_AXIAL	AX_T1_POST_15	AX_T1_15
M10 + M14	534	22.02 (KR)	35.70 (SVR)	23.15 (SVR)	28.03 (SVR)	43.37 (KR)
M5 + M10	534	21.74 (KR)	35.57 (SVR)	23.26 (SVR)	28.05 (SVR)	43.42 (KR)
M2 + M10	532	22.02 (KR)	35.72 (SVR)	23.15 (SVR)	28.03 (SVR)	43.36 (KR)
M10 + M11	512	22.51 (KR)	35.86 (SVR)	23.21 (SVR)	28.06 (SVR)	43.28 (KR)
M1 + M4	499	22.76 (SVR)	36.21 (SVR)	23.19 (SVR)	28.05 (SVR)	43.56 (SVR)
M1 + M5	491	22.10 (SVR)	35.97 (SVR)	23.39 (SVR)	28.06 (SVR)	43.63 (SVR)
M4 + M14	487	22.74 (SVR)	36.23 (SVR)	23.25 (SVR)	28.07 (SVR)	43.58 (SVR)
M4 + M5	487	22.37 (SVR)	36.21 (SVR)	23.40 (SVR)	28.05 (SVR)	43.71 (SVR)
M5 + M13	486	22.07 (SVR)	35.90 (SVR)	23.44 (SVR)	28.07 (SVR)	43.63 (SVR)
M4 + M11	481	23.05 (SVR)	36.92 (SVR)	23.29 (SVR)	28.06 (SVR)	43.56 (KR)

Table 8. R^2 values of regression models on the fastMRI dataset with 1.5 Tesla acquisition.

Metrics	Score	T1_AXIAL_POST_GAD	Axial_T1_SE	T1_AXIAL	AX_T1_POST_15	AX_T1_15
M2 + M10	539	0.9386 (KR)	0.8503 (SVR)	0.9327 (SVR)	0.8642 (SVR)	0.7304 (KR)
M5 + M10	537	0.9404 (KR)	0.8517 (SVR)	0.9325 (SVR)	0.8642 (SVR)	0.7298 (KR)
M10 + M14	536	0.9387 (KR)	0.8500 (SVR)	0.9328 (SVR)	0.8642 (SVR)	0.7303 (KR)
M1 + M5	508	0.9371 (SVR)	0.8466 (SVR)	0.9317 (KR)	0.8643 (SVR)	0.7271 (RF)
M5 + M13	500	0.9372 (SVR)	0.8467 (SVR)	0.9316 (KR)	0.8642 (SVR)	0.7268 (RF)
M10 + M11	489	0.9337 (KR)	0.8453 (SVR)	0.9323 (SVR)	0.8636 (SVR)	0.7317 (KR)
M4 + M5	488	0.9353 (SVR)	0.8430 (SVR)	0.9313 (SVR)	0.8644 (SVR)	0.7253 (RF)
M1 + M6	487	0.9399 (SVR)	0.8355 (SVR)	0.9341 (KR)	0.8601 (SVR)	0.7310 (RF)
M2 + M13	481	0.9346 (SVR)	0.8374 (SVR)	0.9316 (SVR)	0.8642 (SVR)	0.7279 (RF)
M2 + M4	480	0.9330 (SVR)	0.8440 (SVR)	0.9316 (SVR)	0.8642 (SVR)	0.7262 (RF)

Table 9. Goodness-of-fit of noise level regression in the fastMRI dataset with 3 Tesla acquisition. The metrics are globally ranked by the *MSE* value, scaled up by a factor of 10^4 in this table.

Metrics	Score	AX_T1_FLASH_(POST)	AX_T1_POST_3	AX_T1_3
M11 + M13	348	7.41 (KR)	22.30 (RF)	25.62 (KR)
M5 + M10	344	7.60 (KR)	19.46 (KR)	26.06 (KR)
M10 + M11	342	7.42 (KR)	22.29 (RF)	26.08 (KR)
M1 + M11	342	7.44 (KR)	22.31 (RF)	25.83 (KR)
M4 + M11	338	7.50 (KR)	22.39 (RF)	25.77 (KR)
M2 + M10	333	7.85 (KR)	19.83 (KR)	26.21 (RF)
M10 + M14	332	7.86 (KR)	19.81 (KR)	26.21 (RF)
M5 + M13	331	7.51 (SVR)	22.23(RF)	26.53 (RF)
M2 + M13	328	7.61 (SVR)	22.36 (RF)	26.13 (RF)
M13 + M14	327	7.59 (SVR)	22.31 (RF)	26.36 (RF)

Table 10. Goodness-of-fit of noise level regression in the fastMRI dataset with 3 Tesla acquisition. The metrics are globally ranked by the MAE value, scaled up by a factor of 10^3 in this table.

Metrics	Score	AX_T1_FLASH_(POST)	AX_T1_POST_3	AX_T1_3
M2 + M10	345	19.10 (KR)	31.59 (KR)	39.33 (RF)
M10 + M14	343	19.11 (KR)	31.59 (KR)	39.34 (RF)
M5 + M10	340	19.10 (KR)	31.43 (KR)	39.56 (KR)
M2 + M13	339	19.52 (SVR)	31.68 (SVR)	39.20 (RF)
M1 + M14	338	19.50 (SVR)	31.67 (SVR)	39.30 (RF)
M1 + M2	332	19.51 (SVR)	31.68 (SVR)	39.33 (RF)
M11 + M13	331	18.90 (KR)	32.22 (SVR)	39.13 (KR)
M13 + M14	327	19.52 (SVR)	31.68 (SVR)	39.37 (RF)
M5 + M13	326	19.41 (SVR)	31.61 (SVR)	39.78 (RF)
M10 + M11	325	18.96 (KR)	32.42 (RF)	39.26 (RF)

Table 11. R^2 of regression models on the fastMRI dataset with 3 Tesla acquisition.

Metrics	Score	AX_T1_FLASH_(POST)	AX_T1_POST_3	AX_T1_3
M11 + M13	348	0.9433 (KR)	0.8499 (RF)	0.8009 (KR)
M1 + M11	342	0.9448 (KR)	0.8527 (RF)	0.8020 (KR)
M10 + M11	342	0.9432 (KR)	0.8500 (RF)	0.8009 (KR)
M5 + M10	342	0.9457 (KR)	0.8316 (KR)	0.7973 (KR)
M4 + M11	338	0.9457 (KR)	0.8318 (RF)	0.7984 (KR)
M10 + M14	333	0.9464 (KR)	0.8313 (KR)	0.8018 (RF)
M2 + M10	332	0.9449 (KR)	0.8320 (KR)	0.7961 (RF)
M5 + M13	330	0.9428 (SVR)	0.8280 (KR)	0.7948 (RF)
M2 + M13	329	0.9450 (SVR)	0.8308 (KR)	0.8015 (RF)
M13 + M14	327	0.9446 (SVR)	0.8315 (KR)	0.7987 (RF)

4.1. Mindboggle

Table 3 collects MSE values for the metrics, taking into account the score of the analysis represented in Tables S1, S4, S7, S10 and S13. The best input is the combination **M1** + **M3** for all repositories with a score of 473. **M1** + **M3** yields the best results because the spread of the input samples for the regression is smaller for that combination, which facilitates the learning of the underlying Rician noise level function. This lower spread can be observed if Figures 15–19 corresponding to the **M1** + **M3** combination are compared with, for example, Figures 7, 8, 20 and 21, which correspond to other combinations. The latter figures exhibit a higher spread in the values of the inputs **Mi**, **Mj** as compared with the spread of the inputs **Mi**, **Mj** of the former. Therefore, it is easier to learn the underlying Rician noise level function. The MMRR dataset shows better performance using the SVR regressor. It is followed by the HLN dataset as a result of the use of KR. Next, OASIS-TRT shows MSE results using RF, KR and SVR, depending on the metrics used as input. It is followed by the NKI-RS dataset, and finally, the worst results are for NKI-TRT, with both of the models using PR.

In the same way, Table 4 shows MAE values for different metrics and repositories. This information is a summary of the information in the Tables S2, S5, S8, S11 and S14. The best metric for all repositories is **M12** + **M13** with a score of 499. The combination **M1** + **M3** for MSE mentioned above is in seventh place with a score of 473. The order of results for datasets is the same as for MSE described in the above paragraph: MMRR with SVR; HLN using PR, SVR, and KR; OASIS-TRT with KR and RF; NKI-RS with RF; and NKI-TRT with SVM.

Finally, Table 5 abridges the information of Tables S3, S6, S9, S12 and S15. **M1** + **M3** is the best input with a score of 477. The results show the same order in the repositories: MMRR with SVR; HLN using KR, SVR, and PR; OASIS-TRT with RF and KR; NKI-RS with PR and RF, and NKI-TRT with PR.
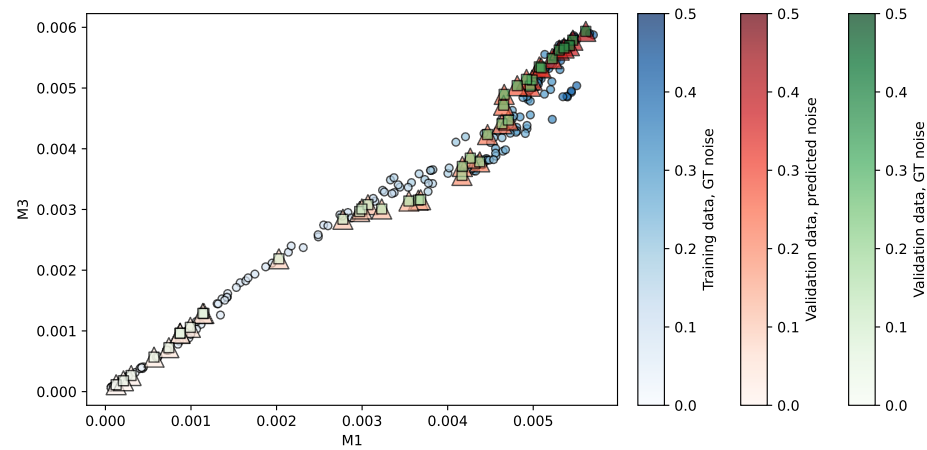
Figure 15. Regression of the HLN repository using SVR (best ranked model). Predictors are (M1, M3). The opacity of each shape indicates the noise level associated.
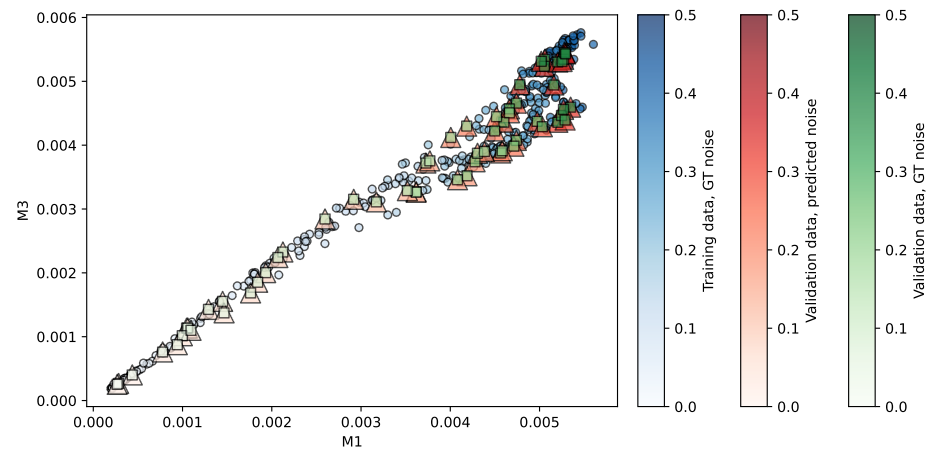

Figure 16. Regression of the MMRR repository using SVR (best ranked model). Predictors are (M1, M3). The opacity of each shape indicates the noise level associated.
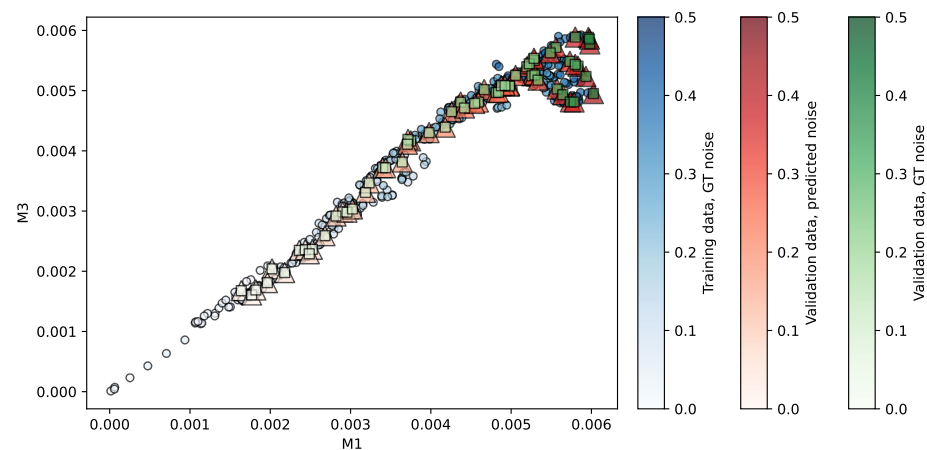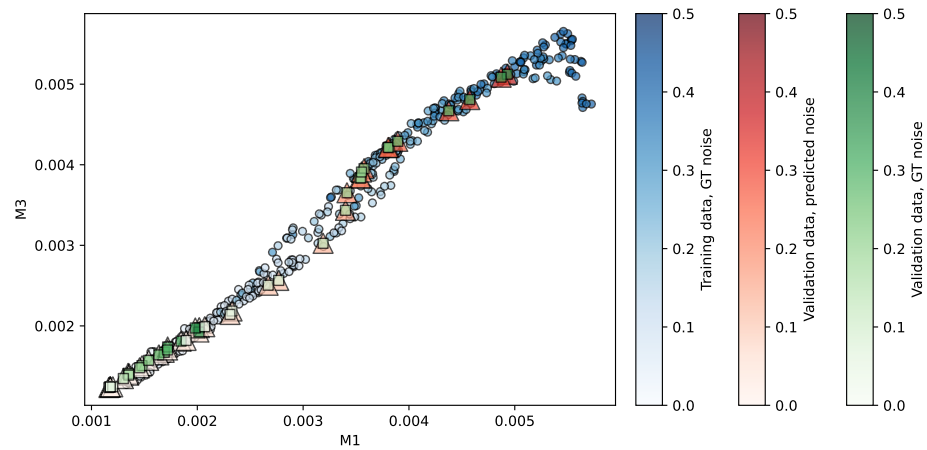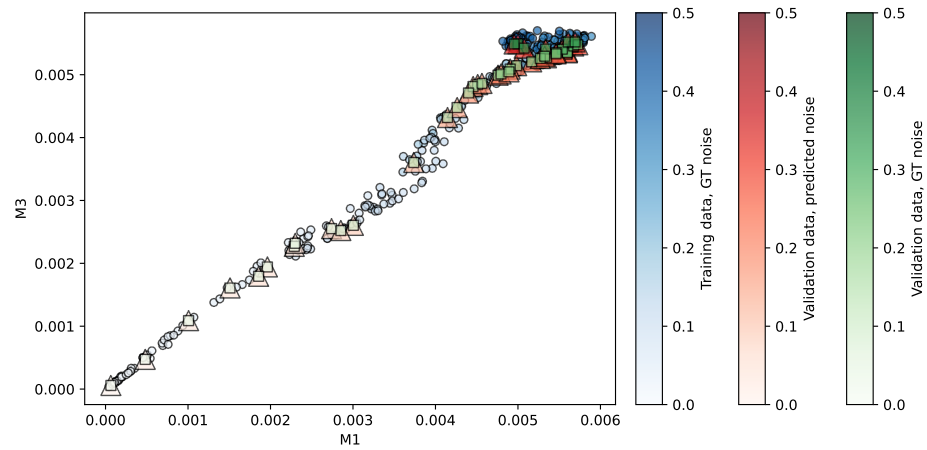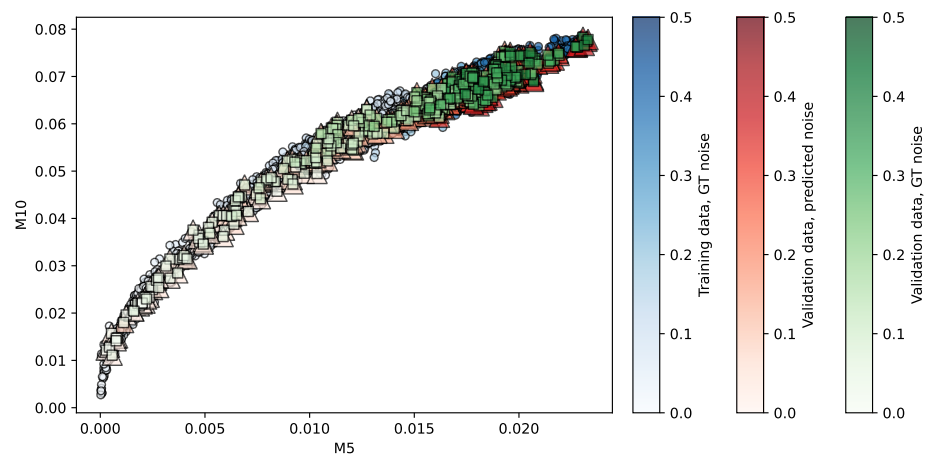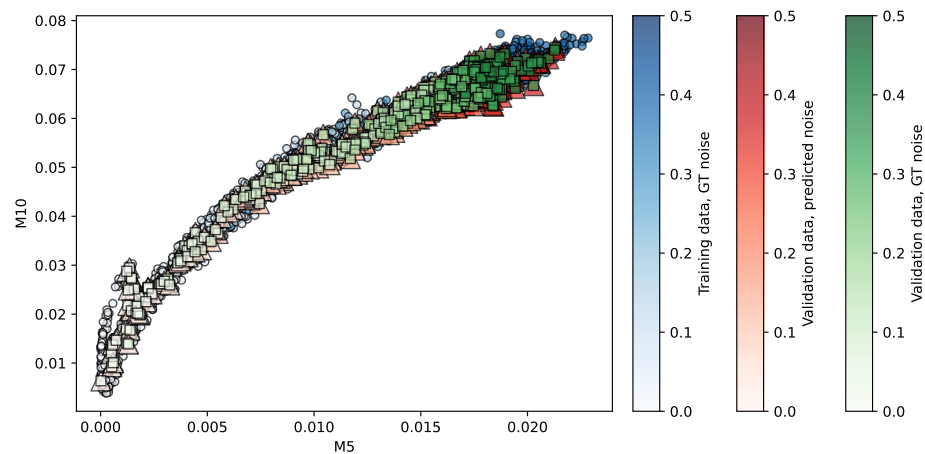

Figure 17. Regression of the NKI-RS repository using SVR (best ranked model). Predictors are (M1, M3). The opacity of each shape indicates the noise level associated.

Figure 18. Regression of the NKI-TRT repository using SVR (best ranked model). Predictors are $(M1, M3)$. The opacity of each shape indicates the noise level associated.

Figure 19. Regression of the OASIS-TRT repository using SVR (best ranked model). Predictors are $(M1, M3)$. The opacity of each shape indicates the noise level associated.

Figure 20. Regression of the AX-T1-1.5 dataset using SVR (best ranked model). Predictors are $(M5, M10)$. The opacity of each shape indicates the noise level associated.

Figure 21. Regression of the AX-T1-POST-1.5 dataset using SVR (best ranked model). Predictors are (M5, M10). The opacity of each shape indicates the noise level associated.

To reach a consensus, the score of the different performance measures were added to obtain the best input metric; see Table 12. The top-scoring metric is **M1 + M3** with a score of 1423. When analyzing this metric around all repositories, SVR works better. Therefore, **M1 + M3** as an input using SVR is our chosen model as the best performing one. The results of using this model are shown in Figures 15–19.

Table 12. Metrics sorted by score according to the performance measures using MRIs from the Mindboggle dataset.

Metrics	Score
M1 + M3	1423
M1 + M15	1408
M3 + M13	1407
M3 + M4	1404
M4 + M15	1399
M13 + M15	1379
M12 + M13	1353
M1 + M11	1343
M1 + M12	1342
M11 + M13	1337

This model is compared with the VST model to check the precision to estimate Rician noise (see Table 13). Independent of the repository used, the proposed model improves the results of the VST model. Using the HLN dataset, the VST model has $R^2 = 0.86$. Therefore, it works worse than the proposed model with $R^2 = 0.98$. Using the OASIS-TRT dataset, the value of $R^2 = 0.87$ indicates that the proposed model works better with $R^2 = 0.94$. For the rest of the repositories, the VST model cannot predict the Rician noise, whereas the proposed model predicts the noise for MMRR with a value of $R^2 = 0.98$ and, when using NKI-RS, with $R^2 = 0.91$. NKI-TRT shows $R^2 = 0.68$, which coincides with what is described in the tables of the previous section. This repository does not produce good results in the prediction. Applying the VST method also reflects this in their outcomes. It is demonstrated that our model improves noise prediction results compared with what is currently available in the literature.

Table 13. Metrics sorted by score according to the performance measures, using MRIs from the fastMRI dataset with 1.5 Tesla acquisition.

Metrics	Score
M5 + M10	1601
M2 + M10	1598
M10 + M14	1595
M1 + M5	1517
M5 + M13	1497
M10 + M11	1477
M4 + M5	1461
M2 + M4	1454
M2 + M13	1446
M13 + M14	1437

The HLN repository shows KR as a better model taking into the value of $R^2 = 0.98$ (see Table S3). It determines M4 as the best metric (see Figure 2). On the other hand, the M1 option is positioned at the bottom of the score, indicating that the metrics used in this analysis outperform the previous results in [30]. With good precision, $R^2 = 0.98$ determines SVR as the best model for the MMRR repository (see Table S6). The metrics M1 and M2 as the input in the model are the most successful results (see Figure 3). PR is the best model for MSE value and $R^2 = 0.91$ for the NKI-RS repository (see Table S9). The combination of M4 and M5 is the most successful (see Figure 4). The NKI-TRT dataset shows LR as a better model if the check $R^2 = 0.71$ (see Table S12). The model's most significant achievements are attributed to using metrics M6 and M15 as inputs (see Figure 5). According to the OASIS repository, KR is the most significant model when considering the MSE, MAE, and $R^2 = 0.95$ (see Tables S13–S15). The model accomplishes its greatest success when utilizing the metrics M5 and M8 as inputs (see Figure 6).

4.2. fastMRI-1.5

Table 6 collects *MSE* values for the metrics, taking into account the score of the analysis represented in the Tables S16, S19, S22, S25 and S28. The best input is the combination **M5** + **M10** for all repositories with a score of 530. The T1-AXIAL-POST-GAD dataset shows better performance using KR and then SVR. It is followed by the T1-AXIAL dataset using SVR and KR, which is followed by AX-T1-POST-1.5 and then the Axial-T1-SE dataset, both of them using SVR. Finally, the AX-T1-1.5 dataset shows *MSE* using KR and RF.

Table 7 shows *MAE* values for different metrics and repositories. This information is a summary of the information in Tables S17, S20, S23, S26 and S29. The best metric for all repositories is **M5** + **M10** with a score of 534. It is the same combination that *MSE* showed before. The order of results for datasets is the same as for *MSE* described in the above paragraph: T1-AXIAL-POST-GAD using the KR and then SVR; T1-AXIAL, AX-T1-POST-1.5, and Axial-T1-SE all with SVR; and AX-T1-1.5 with KR and RF.

Table 8 shows R^2 values for different metrics and repositories. This information is a summary of the information in Tables S18, S21, S24, S27 and S30. The best metric for all repositories is **M2** + **M10** with a score of 539. The combination **M5** + **M10** for *MSE* and *MAE* mentioned above is in second place with a score of 537. The order of results for datasets is the same as for *MSE* and *MAE* described in the above paragraph: T1-AXIAL-POST-GAD using the KR and then SVR; T1-AXIAL with SVR and KR; AX-T1-POST-1.5 and Axial-T1-SE all with SVR; and AX-T1-1.5 with KR and RF.

To reach a consensus, the score of the different performance measures were added to obtain the best input metric (see Table 14). The top-scoring metric is **M5** + **M10** with a score of 1601. Analyzing this metric around all repositories, SVR performs better. Therefore, **M5** + **M10** as an input using SVR is our chosen model as the best performing one. The results of using this model are shown in Figures 20–24.

Table 14. Metrics sorted by score according to the performance measures using MRIs from the fastMRI dataset with 3 Tesla acquisition.

Metrics	Score
M11 + M13	1027
M5 + M10	1026
M2 + M10	1010
M10 + M11	1009
M1 + M11	1008
M10 + M14	1000
M4 + M11	996
M2 + M13	987
M5 + M13	984
M1 + M2	984
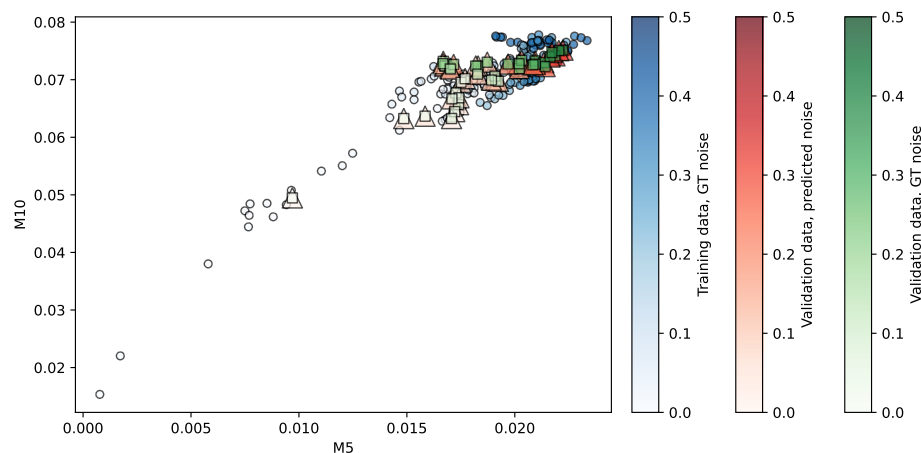
Figure 22. Regression of the AX-T1-SE dataset using SVR (best ranked model). Predictors are $(M5, M10)$. The opacity of each shape indicates the noise level associated.
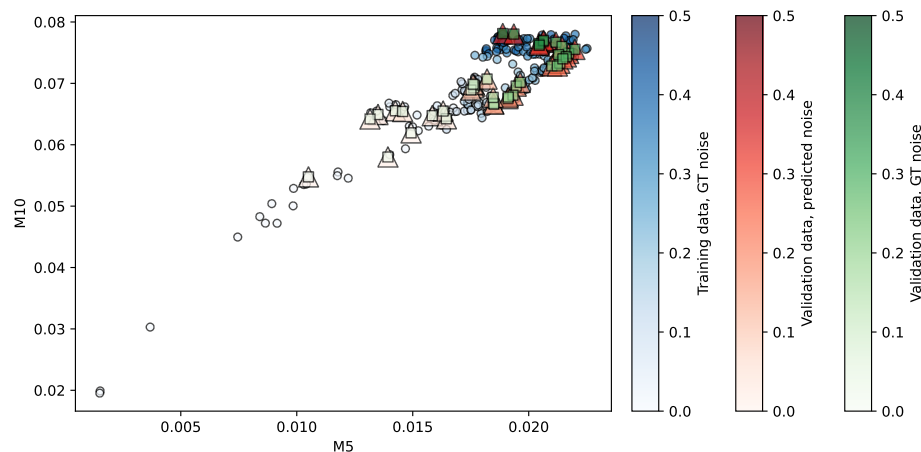
Figure 23. Regression of the T1-AXIAL dataset using SVR (best ranked model). Predictors are $(M5, M10)$. The opacity of each shape indicates the noise level associated.
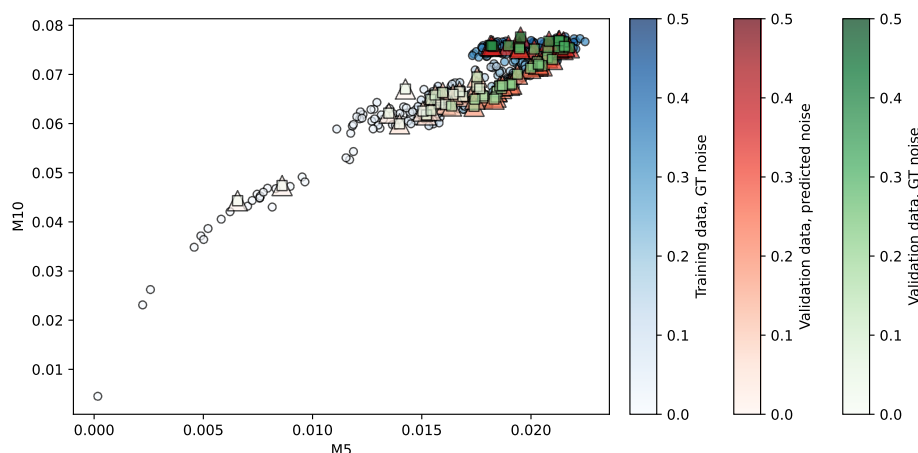
Figure 24. Regression of the T1-AXIAL-POST-GAD dataset using SVR (best ranked model). Predictors are (M5, M10). The opacity of each shape indicates the noise level associated.

This model is compared with the VST model to check the precision to estimate Rician noise (see Table 15). It can be seen that the VST model predicts better than the model we propose when evaluated with this 1.5 Tesla MRI dataset. Paying attention to the R^2 measure for VST, the threshold of one is reached for the three datasets of Axial-T1-SE, T1-AXIAL, and T1-AXIAL-POST-GAD. Our model is also optimistic for the sets of T1-AXIAL-POST-GAD and T1-AXIAL, with a score of $R^2 = 0.93$ in both. For Axial-T1-SE, the accuracy is a little lower, with $R^2 = 0.85$. AX-T1-POST-1.5 demonstrates high precision with $R^2 = 0.99$, and our model shows $R^2 = 0.71$. Finally, AX-T1-POST-1.5 scores $R^2 = 0.98$, and our model presents $R^2 = 0.86$.

Table 15. Comparison between the VST model and the proposed model (predictors are (M1, M3), and the regressor is SVR) based on performance measures. MSE is multiplied by 10^{-4}. MAE is multiplied by 10^{-3}.

Performance Measure	MSE		MAE		R^2	
Model	VST	Ours	VST	Ours	VST	Ours
HLN	18.58	3.31	31.82	13.21	0.86	0.98
MMRR	52.43	2.51	45.91	10.96	0.59	0.98
NKI-RS	80.88	12.17	64.50	26.59	0.38	0.91
NKI-TRT	1007.04	37.83	129.28	6.68	0.00	0.68
OASIS-TRT	17.04	8.02	27.77	20.29	0.87	0.94

The fastMRI-1.5 results are discussed below. The AX-T1-1.5 dataset shows KR as a better model when taking into the value of $R^2 = 0.76$ (see Table S18). It determines M8 + M12 as the best metric (see Figure 7). The precision of $R^2 = 0.87$ determines SVR as the best model for the AX-T1-POST-1.5 repository (see Table S21). The metrics M5 and M9 as the input in the model are the most successful results (see Figure 8). SVR is the best model with the combination of M5 and M10; see Figure 9 for MSE, MAE, and $R^2 = 0.85$. For the Axial-T1-SE dataset, see Tables S22–S24. The T1-AXIAL dataset shows KR as a better model if the check $R^2 = 0.93$ (see Table S27). The model's most significant achievements are attributed to using metrics M1 and M6 as inputs (see Figure 10). According to the T1-AXIAL-POST-GAD repository, KR is the most significant model when considering the MSE, MAE, and $R^2 = 0.94$ (see Tables S28–S30). The model accomplishes its greatest success when utilizing the metrics M6 and M10 as inputs (see Figure 11).

4.3. fastMRI-3

Table 9 collects MSE values for the metrics taking into account the score of the analysis represented in Tables S31, S34 and S37. The best input is the combination **M11** + **M1** for all

repositories with a score of 348. The AX-T1-FLASH-POST dataset shows better performance using KR and then SVR. It is followed by the AX-T1-POST-3 dataset using RF and KR. The last is AX-T1-3 using KR and RF.

Table 10 collects *MSE* values for the metrics, taking into account the score of the analysis represented in Tables S32, S35 and S38. The best input is the combination **M2** + **M10** for all repositories with a score of 345. The combination **M11** + **M13** for *MSE* mentioned above is in seventh place with a score of 431. The order of results for datasets is the same as for *MSE* described in the above paragraph: AX-T1-FLASH-POST-3 with KR and then SVR; AX-T1-POST-3 with KR and SVR; and AX-T1-3 with KR and RF.

Table 11 collects R^2 values for the metrics, taking into account the score of the analysis represented in Tables S33, S36 and S39. The best input is the combination **M11** + **M13** for all repositories with a score of 348. It is the same combination that *MSE* showed before. The order of results for datasets is the same as for *MSE* and *MAE* described in the above paragraph: AX-T1-FLASH-POST-3 with KR and then SVR; AX-T1-POST-3 with KR and KR; and AX-T1-3 with KR and RF.

To reach a consensus, the score of the different performance measures were added to obtain the best input metric (see Table 16). The top-scoring metric is **M11** + **M13** with a score of 1027. Analyzing this metric around all repositories, SVR performs better. Therefore, **M11** + **M13** as the input using SVR is our chosen model as the best performing one. The results of using this model are shown in Figures 25–27.

Table 16. Comparison between the VST model and the proposed model (predictors: $(M5, M10)$, regressor is SVR) based on performance measures. *MSE* is multiplied by 10^{-4}. *MAE* is multiplied by 10^{-3}.

Performance Measure	MSE		MAE		R^2	
Model	VST	Ours	VST	Ours	VST	Ours
AX-T1-1.5	1.71	37.54	4.88	43.71	0.99	0.71
AX-T1-POST-1.5	2.39	17.92	6.66	28.05	0.98	0.86
Axial-T1-SE	0.14	20.71	2.86	35.57	1.00	0.85
T1-AXIAL	0.11	9.56	2.64	23.26	1.00	0.93
T1-AXIAL-POST-GAD	0.10	8.75	2.48	22.35	1.00	0.93

This model is compared with the VST model to assess its precision in estimating Rician noise (see Table 17). It can be seen that the VST model predicts better than the model we propose when evaluated with these 3 Tesla fastMRI datasets. Paying attention to the R^2 measure for VST, the threshold of one is reached for the AX-T1-3 and AX-T1-FLASH-POST dataset. Our model is also optimistic for the AX-T1-FLASH-POST set with $R^2 = 0.94$, and it has lower precision for AX-T1-3 with $R^2 = 0.78$. Finally, AX-T1-POST-3 scores $R^2 = 0.90$ and our model scores $R^2 = 0.81$.

Table 17. Comparison between the VST model and the proposed model (predictors are $(M11, M13)$, regressor is SVR) based on performance measures. *MSE* is multiplied by 10^{-4}. *MAE* is multiplied by 10^{-3}.

Performance Measure	MSE		MAE		R^2	
Model	VST	Ours	VST	Ours	VST	Ours
AX-T1-3	0.13	29.16	2.79	41.53	1.00	0.78
AX-T1-FLASH-POST	0.12	8.03	2.82	19.95	1.00	0.94
AX-T1-POST-3	13.68	24.45	6.72	32.22	0.90	0.81

As a discussion of the fastMRI-3 dataset, the AX-T1-3 dataset shows KR as the best model when taking into the value of $R^2 = 0.80$ (see Table S33). It determines M11 + M13 as the best metric (see Figure 12). The precision of MSE, MAE, and $R^2 = 0.95$ determines KR

as the best model for the AX-T1-FLASH-POST repository with the metrics M11 and M13 (see Figure 8 and see Tables S34–S36). The metrics M5 and M10 as the input in the model (see Figure 14) are the most successful results for AX-T1-POST as indicated by MSE, MAE, and $R^2 = 0.85$ (see Tables S22–S24).
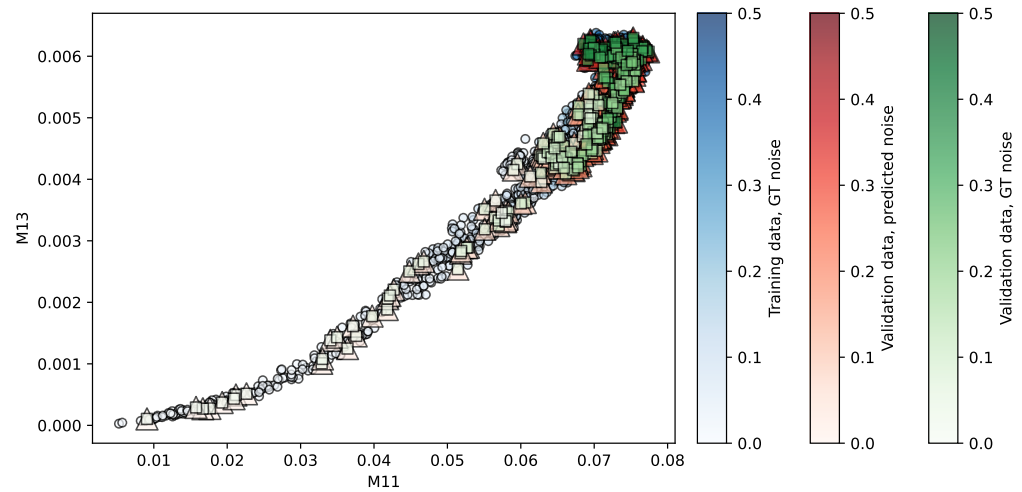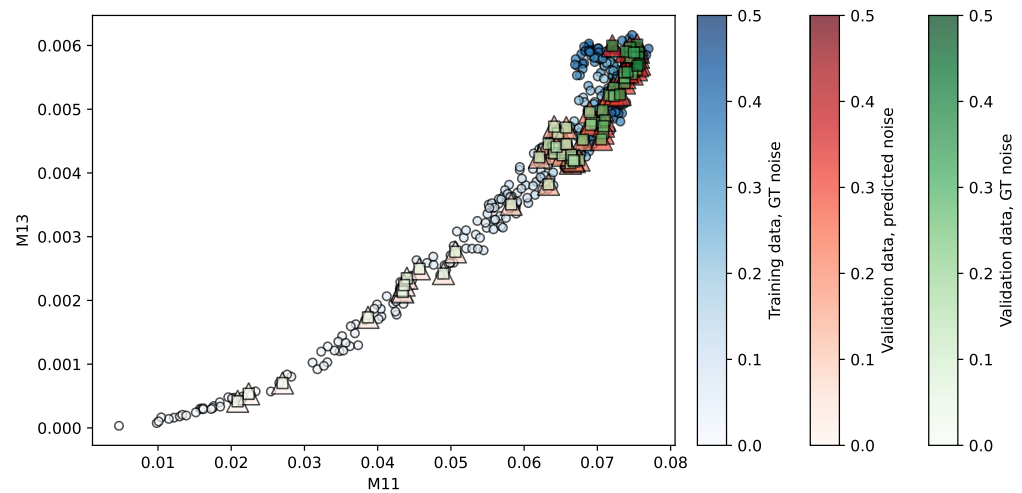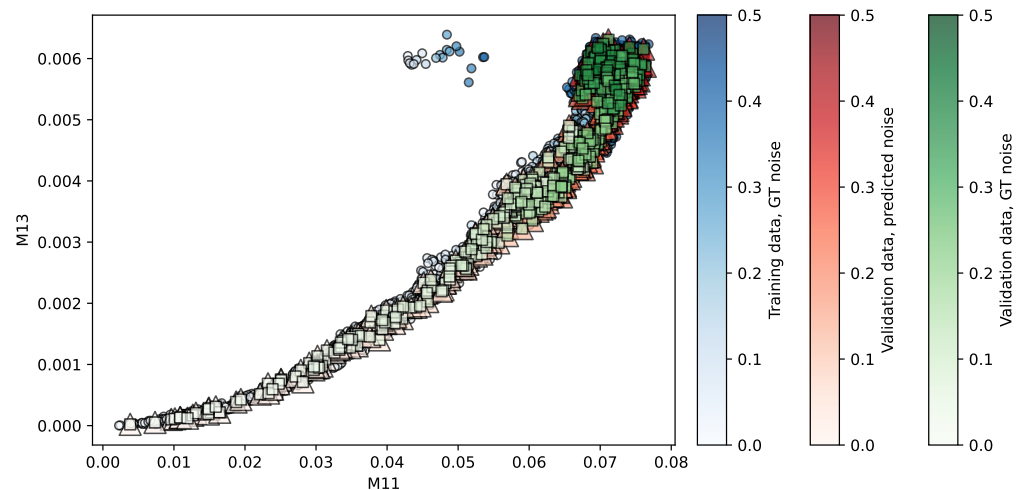

Figure 25. Regression of the AX-T1 dataset with 3 Tesla acquisitions using SVR (best ranked model). Predictors are (M11, M13). The opacity of each shape indicates the noise level associated.

Figure 26. Regression of the AX-T1-FLASH-POST dataset with 3 Tesla acquisitions using SVR (best ranked model). Predictors are (M11, M13). The opacity of each shape indicates the noise level associated.

4.4. Summary

In general, the score of the best performing metrics does not include the single M1 or single M4 metrics. Therefore, we greatly outperform the prior proposal [30].

As seen in Tables 3–5, several combinations of metrics and regressors yield very good results for all Mindboggle MRI datasets. However, there are slight differences among them due to the variety of MRI acquisition parameters and procedures employed for each dataset. The best combinations of metrics and regressors overall, i.e., considering all real datasets, are reported in Table 12. According to these data, the metrics M1 + M3 yield the best results when combined with the SVR regressor. This combination has been employed for the comparisons reported in Table 15.

Figure 27. Regression of the AX-T1-POST dataset with 3 Tesla acquisitions using SVR (best ranked model). Predictors are (M11, M13). The opacity of each shape indicates the noise level associated.

On the other hand, multiple combinations of metrics and regressors produce satisfactory results for all fastMRI datasets with 1.5 Tesla acquisition (see Tables 6–8) and with 3 Tesla acquisition (see Tables 9–11). Nevertheless, subtle differences exist due to different MRI dimensions, acquisition parameters, and procedures. The most satisfactory combinations of metrics and regressors considering the fastMRI dataset with 1.5 Tesla and 3 Tesla acquisitions are reported in Tables 13 and 14, respectively.

Finally, when comparing the proposed model based on Benford's law with respect to the VST model, the results depicted in Tables 13, 15 and 17 demonstrate that our model is suitable for use with different types of datasets as the performance is good among any image sequence, having an average R^2 value of 0.87 among all datasets. However, although VST presents an excellent performance with fastMRI images, it lacks enough precision with Mindboggle, achieving an average R^2 value of 0.81, and sometimes with a really inexact estimation of the noise. Therefore, our proposal seems valid regardless of the MRI analyzed.

5. Conclusions

This study unveils compelling insights into the distribution characteristics of coefficients obtained from various transforms applied to T1 MRI images. Specifically, we demonstrate the adherence of Fourier, discrete cosine, and discrete sine transform coefficients to Benford's law, which manifests as a logarithmic distribution of their first digits. Furthermore, this investigation highlights the influence of Rician noise on the first digit distribution of the above coefficients, causing deviations from Benford's ideal distribution. Consequently, a novel methodology is proposed that leverages various metrics such as the Bhattacharyya distance, Kullback–Leibler divergence, total variation distance, Hellinger distance, and Jensen–Shannon divergence to assess the level of noise in T1 MRI images based on the agreement between the first digit distribution of coefficients and Benford's law.

In particular, this paper explored the potential of supervised learning techniques in estimating noise levels by utilizing the aforementioned divergence metrics as regressors. Despite variations in the quality of the datasets, the experiments involving MRI scans from several datasets coming from a wide range of different acquisition devices of 1.5 Tesla and 3 Tesla, comprising hundreds of patients, consistently validate the adherence of noiseless T1 MRI Fourier coefficients to Benford's law. Moreover, the observed consistency in error measures further supports the accurate estimation of noise levels, being competitive with and even outperforming other well-known techniques, such as the variance stabilization transform (VST).

Incorporating our methodology into existing MRI systems and diagnostic tools can have an impact on the field of medical imaging. It not only enhances the quality and accu-

racy of images but also enables the development of more robust AI-driven diagnostic tools. Additionally, it provides a standardized and data-driven approach to noise estimation, which is vital for the medical community. This fusion has the potential to significantly refine the quality of MRI images, augment diagnostic capabilities, improve patient care, and streamline the clinical workflow in the realm of medical imaging.

Integrating the approach from this paper into existing MRI systems and diagnostic tools involves a process that harmonizes innovative methodology with established technology. It would begin with the development of software modules or plugins, designed to seamlessly merge with current MRI systems and diagnostic software. These modules would undertake crucial data preprocessing, extracting essential image transform coefficients such as Fourier, discrete cosine, and discrete sine transforms that are essential for subsequent noise estimation based on Benford's law.

The heart of this integration lies in the seamless integration of the noise estimation algorithm into the existing framework. Using Benford's law and the metrics proposed in the study, such as Bhattacharyya distance and Kullback–Leibler divergence, the algorithm would estimate the noise deviation parameter from the transformed coefficients. It is not merely about computation but also about translating the outcomes of noise estimation into practical usage. The integration involves aligning these outcomes with denoising algorithms within the MRI system, effectively refining them to preserve critical diagnostic information while enhancing overall image quality. Note that our proposal presents a consistent performance across diverse MRI datasets and acquisition devices.

This amalgamation would not stop at technical integration; it should bring a user-friendly interface to radiologists and clinicians, ensuring the estimated noise level and its impact on image quality are presented clearly and comprehensibly. This would result in highly usable systems in practical situations.

To summarize, this work provides empirical evidence supporting the hypothesis of Benford's law in several domains, presenting a novel application of transform coefficients and their adherence to Benford's law as a reliable noise estimator. The utilization of divergence metrics showcases promising results and demonstrates the potential for advancing image quality assessment.

the Universidad de Málaga and the Instituto de Investigación Biomédica de Málaga y Plataforma en Nanomedicina-IBIMA Plataforma BIONAND.

Data Availability Statement: MRI from Mindboggle [44] are publicly accessible with a non-restrictive license: http://mindboggle.info/data (accessed on 1 March 2023). Dataset was downloaded from https://osf.io/9ahyp/ (accessed on 1 July 2023). The fastMRI dataset [45] are available at https://fastmri.med.nyu.edu/ (accessed on 1 March 2023).

Conflicts of Interest: The authors declare no conflict of interest.

References

1. Alymani, M.; Alhazmi, M.H.; Almarhabi, A.; Alhazmi, H.; Samarkandi, A.; Yao, Y.D. Rician K-factor estimation using deep learning. In Proceedings of the 2020 29th Wireless and Optical Communications Conference (WOCC), Newark, NJ, USA, 1–2 May 2020; pp. 1–4.
2. Salhab, A.M.; Samuh, M.H. Accurate performance analysis of reconfigurable intelligent surfaces over Rician fading channels. *IEEE Wirel. Commun. Lett.* **2021**, *10*, 1051–1055. [CrossRef]
3. Acar, Y.E.; Seflek, I.; Yaldız, E. Wavelet based denoising of the simulated chest wall motion detected by SFCW radar. *Adv. Electromagn.* **2019**, *8*, 85–91. [CrossRef]
4. Fon, R.C.; Ndjiongue, A.R.; Ouahada, K. Cascaded optic fibre–visible light communications: Channel model and analysis. In Proceedings of the 2019 International Conference on Advances in Big Data, Computing and Data Communication Systems (icABCD), Winterton, South Africa, 5–6 August 2019; pp. 1–6.
5. Gudbjartsson, H.; Patz, S. The Rician distribution of noisy MRI data. *Magn. Reson. Med.* **1995**, *34*, 910–914. [CrossRef] [PubMed]
6. Yang, X.; Fei, B. A wavelet multiscale denoising algorithm for magnetic resonance (MR) images. *Meas. Sci. Technol.* **2011**, *22*, 025803. [CrossRef]
7. Krissian, K.; Aja-Fernández, S. Noise-driven anisotropic diffusion filtering of MRI. *IEEE Trans. Image Process.* **2009**, *18*, 2265–2274. [CrossRef]
8. Rajan, J.; Jeurissen, B.; Verhoye, M.; Van Audekerke, J.; Sijbers, J. Maximum likelihood estimation-based denoising of magnetic resonance images using restricted local neighborhoods. *Phys. Med. Biol.* **2011**, *56*, 5221. [CrossRef]
9. Golshan, H.M.; Hasanzadeh, R.P.; Yousefzadeh, S.C. An MRI denoising method using image data redundancy and local SNR estimation. *Magn. Reson. Imaging* **2013**, *31*, 1206–1217. [CrossRef]
10. Zhang, X.; Xu, Z.; Jia, N.; Yang, W.; Feng, Q.; Chen, W.; Feng, Y. Denoising of 3D magnetic resonance images by using higher-order singular value decomposition. *Med. Image Anal.* **2015**, *19*, 75–86. [CrossRef]
11. Chen, W.; You, J.; Chen, B.; Pan, B.; Li, L.; Pomeroy, M.; Liang, Z. A sparse representation and dictionary learning based algorithm for image restoration in the presence of Rician noise. *Neurocomputing* **2018**, *286*, 130–140. [CrossRef]
12. Yu, H.; Ding, M.; Zhang, X. Laplacian eigenmaps network-based nonlocal means method for MR image denoising. *Sensors* **2019**, *19*, 2918. [CrossRef]
13. Pankaj, D.; Govind, D.; Narayanankutty, K.A. A novel method for removing Rician noise from MRI based on variational mode decomposition. *Biomed. Signal Process. Control* **2021**, *69*, 102737. [CrossRef]
14. Dolz, J.; Betrouni, N.; Quidet, M.; Kharroubi, D.; Leroy, H.A.; Reyns, N.; Massoptier, L.; Vermandel, M. Stacking denoising auto-encoders in a deep network to segment the brainstem on MRI in brain cancer patients: A clinical study. *Comput. Med. Imaging Graph.* **2016**, *52*, 8–18. [CrossRef] [PubMed]
15. Kwon, K.; Kim, D.; Park, H. A parallel MR imaging method using multilayer perceptron. *Med. Phys.* **2017**, *44*, 6209–6224. [CrossRef]
16. Tripathi, P.C.; Bag, S. CNN-DMRI: A convolutional neural network for denoising of magnetic resonance images. *Pattern Recognit. Lett.* **2020**, *135*, 57–63. [CrossRef]
17. Tian, C.; Xu, Y.; Li, Z.; Zuo, W.; Fei, L.; Liu, H. Attention-guided CNN for image denoising. *Neural Netw.* **2020**, *124*, 117–129. [CrossRef] [PubMed]
18. Zhang, K.; Zuo, W.; Chen, Y.; Meng, D.; Zhang, L. Beyond a gaussian denoiser: Residual learning of deep cnn for image denoising. *IEEE Trans. Image Process.* **2017**, *26*, 3142–3155. [CrossRef] [PubMed]
19. Jifara, W.; Jiang, F.; Rho, S.; Cheng, M.; Liu, S. Medical image denoising using convolutional neural network: A residual learning approach. *J. Supercomput.* **2019**, *75*, 704–718. [CrossRef]
20. Datta, P.; Rohilla, R. Denoising Magnetic Resonance Images with Rician Noise Based On Deep Learning. In Proceedings of the 2022 International Conference on Computational Intelligence and Sustainable Engineering Solutions (CISES), Greater Noida, India, 20–21 May 2022; pp. 545–550. [CrossRef]
21. Liu, X.; Tanaka, M.; Okutomi, M. Noise level estimation using weak textured patches of a single noisy image. In Proceedings of the 2012 19th IEEE International Conference on Image Processing, Orlando, FL, USA, 30 September–3 October 2012; pp. 665–668.
22. Chang, S.G.; Yu, B.; Vetterli, M. Spatially adaptive wavelet thresholding with context modeling for image denoising. *IEEE Trans. Image Process.* **2000**, *9*, 1522–1531. [CrossRef]
23. Koay, C.G.; Basser, P.J. Analytically exact correction scheme for signal extraction from noisy magnitude MR signals. *J. Magn. Reson.* **2006**, *179*, 317–322. [CrossRef]

24. Jolion, J.M. Images and Benford's law. *J. Math. Imaging Vis.* **2001**, *14*, 73–81. [CrossRef]

25. Sanches, J.; Marques, J.S. Image Reconstruction using the Benford Law. In Proceedings of the 2006 International Conference on Image Processing, Atlanta, GA, USA, 8–11 October 2006; pp. 2029–2032. [CrossRef]

26. Al-Bandawi, H.; Deng, G. Classification of image distortion based on the generalized Benford's law. *Multimed. Tools Appl.* **2019**, *78*, 25611–25628. [CrossRef]

27. da Silva Azevedo, C.; Gonçalves, R.F.; Gava, V.L.; de Mesquita Spinola, M. A Benford's Law based methodology for fraud detection in social welfare programs: Bolsa Familia analysis. *Phys. A Stat. Mech. Appl.* **2021**, *567*, 125626. [CrossRef]

28. Eckhartt, G.M.; Ruxton, G.D. Investigating and preventing scientific misconduct using Benford's Law. *Res. Integr. Peer Rev.* **2023**, *8*, 1. [CrossRef] [PubMed]

29. Varga, D. Analysis of Benford's Law for No-Reference Quality Assessment of Natural, Screen-Content, and Synthetic Images. *Electronics* **2021**, *10*, 2378. [CrossRef]

30. Maza-Quiroga, R.; Thurnhofer-Hemsi, K.; López-Rodríguez, D.; López-Rubio, E. Rician Noise Estimation for 3D Magnetic Resonance Images Based on Benford's Law. In Proceedings of the Medical Image Computing and Computer Assisted Intervention—MICCAI 2021, Strasbourg, France, 27 September–1 October 2021; Strasbourgde Bruijne, M., Cattin, P.C., Cotin, S., Padoy, N., Speidel, S., Zheng, Y., Essert, C., Eds.; Springer: Cham, Switzerland, 2021; pp. 340–349.

31. Miller, S.J. (Ed.) *Benford's Law: Theory and Applications*; Princeton University Press: Princeton, NJ, USA, 2015.

32. Hill, T.P. A Statistical Derivation of the Significant-Digit Law. *Stat. Sci.* **1995**, *10*, 354–363. [CrossRef]

33. Smith, S.W. *The Scientist & Engineer's Guide to Digital Signal Processing*; California Technical Publishing: San Diego, CA, USA, 1997.

34. Bonettini, N.; Bestagini, P.; Milani, S.; Tubaro, S. On the use of Benford's law to detect GAN-generated images. In Proceedings of the 2020 25th international Conference on Pattern Recognition (ICPR), Milan, Italy, 10–15 January 2020.

35. Milani, S.; Tagliasacchi, M.; Tubaro, S. Discriminating multiple JPEG compressions using first digit features. *APSIPA Trans. Signal Inf. Process.* **2014**, *3*, e19. [CrossRef]

36. Pasquini, C.; Boato, G.; Perez-Gonzalez, F. Statistical Detection of JPEG Traces in Digital Images in Uncompressed Formats. *IEEE Trans. Inf. Forensics Secur.* **2017**, *12*, 2890–2905. [CrossRef]

37. Satapathy, G.; Bhattacharya, G.; Puhan, N.B.; Ho, A.T.S. Generalized Benford's Law for Fake Fingerprint Detection. In Proceedings of the 2020 IEEE Applied Signal Processing Conference (ASPCON), Kolkata, India, 7–9 October 2020; pp. 242–246. [CrossRef]

38. Britanak, V.; Yip, P.C.; Rao, K. Chapter 2—Definitions and General Properties. In *Discrete Cosine and Sine Transforms*; Britanak, V., Yip, P.C., Rao, K., Eds.; Academic Press: Oxford, UK, 2007; pp. 16–50.

39. Kailath, T. The Divergence and Bhattacharyya Distance Measures in Signal Selection. *IEEE Trans. Commun. Technol.* **1967**, *15*, 52–60. [CrossRef]

40. Kullback, S.; Leibler, R.A. On Information and Sufficiency. *Ann. Math. Stat.* **1951**, *22*, 79–86. [CrossRef]

41. Bhattacharyya, A.; Gayen, S.; Meel, K.S.; Myrisiotis, D.; Pavan, A.; Vinodchandran, N.V. On Approximating Total Variation Distance. In Proceedings of the Thirty-Second International Joint Conference on Artificial Intelligence, Macao, China, 9–25 August 2023.

42. Lucien Le Cam, G.L.Y. *Asymptotics in Statistics: Some Basic Concepts*; Springer: New York, NY, USA, 2012.

43. Endres, D.; Schindelin, J. A new metric for probability distributions. *IEEE Trans. Inf. Theory* **2003**, *49*, 1858–1860. [CrossRef]

44. Klein, A.; Tourville, J. 101 Labeled Brain Images and a Consistent Human Cortical Labeling Protocol. *Front. Neurosci.* **2012**, *6*, 171. [CrossRef] [PubMed]

45. Zbontar, J.; Knoll, F.; Sriram, A.; Murrell, T.; Huang, Z.; Muckley, M.J.; Defazio, A.; Stern, R.; Johnson, P.; Bruno, M.; et al. fastMRI: An Open Dataset and Benchmarks for Accelerated MRI. *arXiv* **2018**, arXiv:1811.08839.

46. Morgan, V.L.; Mishra, A.; Newton, A.T.; Gore, J.C.; Ding, Z. Integrating Functional and Diffusion Magnetic Resonance Imaging for Analysis of Structure-Function Relationship in the Human Language Network. *PLoS ONE* **2009**, *4*, e6660. [CrossRef] [PubMed]

47. Landman, B.A.; Huang, A.J.; Gifford, A.; Vikram, D.S.; Lim, I.A.L.; Farrell, J.A.; Bogovic, J.A.; Hua, J.; Chen, M.; Jarso, S.; et al. Multi-parametric neuroimaging reproducibility: A 3-T resource study. *Neuroimage* **2011**, *54*, 2854–2866. [CrossRef]

48. Nooner, K.B.; Colcombe, S.; Tobe, R.; Mennes, M.; Benedict, M.; Moreno, A.; Panek, L.; Brown, S.; Zavitz, S.; Li, Q.; et al. The NKI-Rockland sample: A model for accelerating the pace of discovery science in psychiatry. *Front. Neurosci.* **2012**, *6*, 152. [CrossRef]

49. Marcus, D.S.; Wang, T.H.; Parker, J.; Csernansky, J.G.; Morris, J.C.; Buckner, R.L. Open Access Series of Imaging Studies (OASIS): Cross-sectional MRI Data in Young, Middle Aged, Nondemented, and Demented Older Adults. *J. Cogn. Neurosci.* **2007**, *19*, 1498–1507. Available online: https://direct.mit.edu/jocn/article-pdf/19/9/1498/1936514/jocn.2007.19.9.1498.pdf (accessed on 8 November 2023). [CrossRef]

50. Coupé, P.; Manjón, J.V.; Gedamu, E.; Arnold, D.; Robles, M.; Collins, D.L. Robust Rician noise estimation for MR images. *Med. Image Anal.* **2010**, *14*, 483–493. [CrossRef]

51. Foi, A. Noise estimation and removal in MR imaging: The variance-stabilization approach. In Proceedings of the 2011 IEEE International Symposium on Biomedical Imaging: From Nano to Macro, Chicago, IL, USA, 30 March 2011–2 April 2011; pp. 1809–1814. [CrossRef]
52. Marcel, M. Benford_py: A Python Implementation of Benford's Law Tests. 2017. Available online: https://github.com/milcent/benford_py (accessed on 1 March 2023).